Article

Distinct fission signatures predict mitochondrial degradation or biogenesis

Tatjana Kleele[1✉], Timo Rey[1], Julius Winter[1], Sofia Zaganelli[1], Dora Mahecic[1],
Hélène Perreten Lambert[1], Francesco Paolo Ruberto[2], Mohamed Nemir[2], Timothy Wai[3],
Thierry Pedrazzini[2] & Suliana Manley[1✉]

Mitochondrial fission is a highly regulated process that, when disrupted, can alter metabolism, proliferation and apoptosis[1–3]. Dysregulation has been linked to neurodegeneration[3,4], cardiovascular disease[3] and cancer[5]. Key components of the fission machinery include the endoplasmic reticulum[6] and actin[7], which initiate constriction before dynamin-related protein 1 (DRP1)[8] binds to the outer mitochondrial membrane via adaptor proteins[9–11], to drive scission[12]. In the mitochondrial life cycle, fission enables both biogenesis of new mitochondria and clearance of dysfunctional mitochondria through mitophagy[1,13]. Current models of fission regulation cannot explain how those dual fates are decided. However, uncovering fate determinants is challenging, as fission is unpredictable, and mitochondrial morphology is heterogeneous, with ultrastructural features that are below the diffraction limit. Here, we used live-cell structured illumination microscopy to capture mitochondrial dynamics. By analysing hundreds of fissions in African green monkey Cos-7 cells and mouse cardiomyocytes, we discovered two functionally and mechanistically distinct types of fission. Division at the periphery enables damaged material to be shed into smaller mitochondria destined for mitophagy, whereas division at the midzone leads to the proliferation of mitochondria. Both types are mediated by DRP1, but endoplasmic reticulum- and actin-mediated pre-constriction and the adaptor MFF govern only midzone fission. Peripheral fission is preceded by lysosomal contact and is regulated by the mitochondrial outer membrane protein FIS1. These distinct molecular mechanisms explain how cells independently regulate fission, leading to distinct mitochondrial fates.

Qualitatively, fission appears to occur randomly along the length axis of mitochondria (Fig. 1a). We recorded spontaneous mitochondrial dynamics at high temporal and spatial resolution, without pharmacological induction. Structured illumination microscopy imaging of live Cos-7 cells enabled us to precisely determine the fission positions of mitochondria of various shapes and lengths (Fig. 1b, Supplementary Video 1). Analysis of hundreds of spontaneous fissions revealed a nonuniform probability distribution wherein fission locations are bimodally distributed along the relative length of a mitochondrion (Fig. 1c). We term these either 'peripheral' (less than 25% from a tip) or 'midzone' divisions (within the central 50%). Similar results were obtained by considering mitochondrial area instead of length (Extended Data Fig. 1a, b), as expected, as mitochondrial diameter is relatively constant. This distribution was independent of the length of the dividing mitochondria (Extended Data Fig. 1c, d). Because of this bimodality, smaller daughter mitochondria derived from peripheral divisions have a relatively narrow length distribution (1–2 μm) (Extended Data Fig. 1e). Mitochondria that were labelled with inner or outer membrane markers revealed similar bimodal distributions, confirming complete fission (Extended Data Fig. 1f). To test the generality of our observations, we measured fissions in postnatal mouse cardiomyocytes (Fig. 1d,

Supplementary Video 2). Again, we found a bimodal distribution with mitochondria dividing either in the midzone or peripherally (Fig. 1e).

Dysfunction precedes peripheral fission

We wondered whether geometrically distinct fission types reflected underlying physiological differences. Mitochondria are hubs for metabolic functions, that are characterized by distinct physiological and biochemical properties. The potential across the inner membrane drives oxidative phosphorylation, creating a pH difference between matrix and intermembrane spaces. Reactive oxygen species (ROS), a toxic by-product of oxidative phosphorylation, can lead to mitochondrial damage, often accompanied by loss of membrane potential and release of Ca^{2+} and cytochrome c (ref. [14]). We investigated the physiological states preceding mitochondrial fission with fluorescent sensors (Fig. 1f–i). We found that mitochondrial membrane potential as reported by the dye tetramethylrhodamine ethyl ester (TMRE) was reduced before fission in small peripheral daughter mitochondria (Fig. 1f, g, Supplementary Video 3) compared with corresponding large daughter mitochondria or non-dividing mitochondria. By contrast, no differences were observed between daughter mitochondria

[1]Institute of Physics, École Polytechnique Fédérale de Lausanne (EPFL), Lausanne, Switzerland. [2]Experimental Cardiology Unit, Department of Cardiovascular Medicine, University of Lausanne Medical School, Lausanne, Switzerland. [3]Mitochondrial Biology Group, Institut Pasteur, CNRS UMR 3691, Paris, France. ✉e-mail: tatjana.kleele@epfl.ch; suliana.manley@epfl.ch

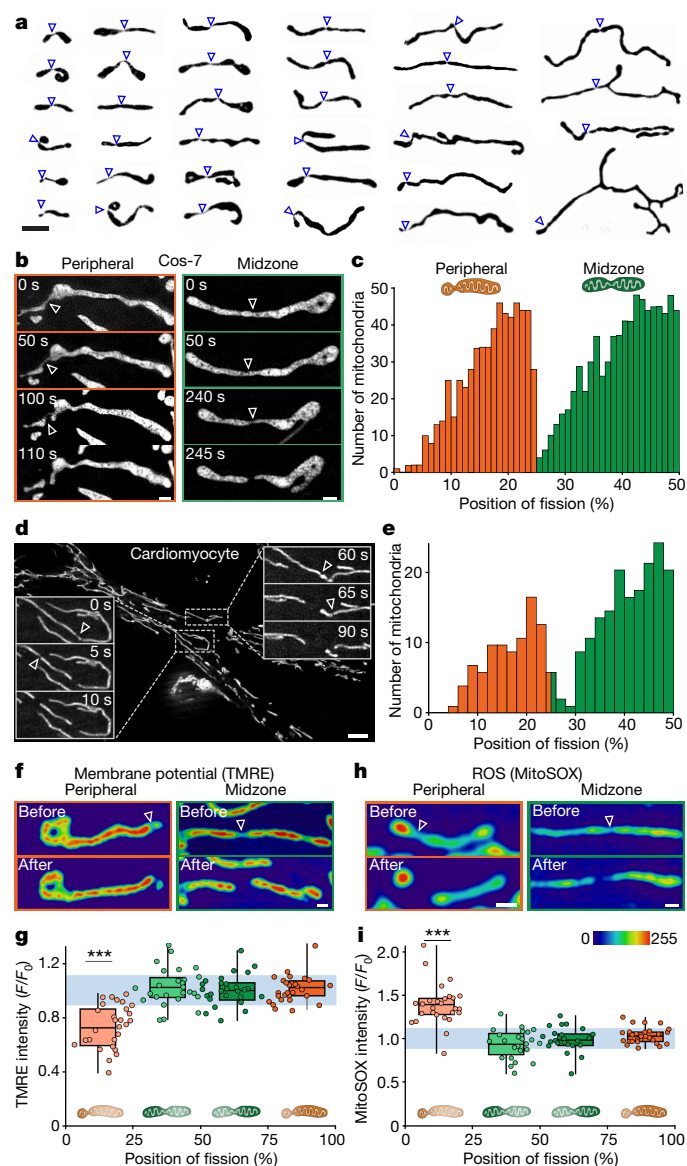**Fig. 1 | Mitochondrial fissions are bimodally positioned and linked to distinct physiologies. a**, Gallery of mitochondria one frame before division from structured illumination microscopy (SIM) movies, binarized. **b**, Time-lapse SIM sequence of a peripheral and a midzone fission of mitochondria (Mitotracker Green). **c**, Histogram of fission positions relative to the total mitochondrial length ($n = 1,393$ fissions pooled from multiple datasets). Fissions occurring near the tip (orange, 0–25%) are termed 'peripheral'; those near the centre (green, 25–50%) are termed 'midzone'. **d**, Instant SIM (iSIM) of mitochondria (Mitotracker Green) in primary mouse cardiomyocytes. Insets: time-lapse sequences from indicated boxes. **e**, Histogram of the relative position of fission in cardiomyocyte mitochondria ($n = 381$ fissions), as in **c**. **f**, Mitochondrial membrane potential before and after a peripheral or midzone fission from SIM movies of tetramethylrhodamine ethyl ester (TMRE)-stained mitochondria. **g**, Normalized TMRE intensity as a function of relative position of fission, measured immediately before fission ($n = 56$ fissions). **h**, MitoSOX labelling reveals ROS levels before and after a peripheral or midzone fission. **i**, Normalized MitoSOX intensity as a function of relative fission position, measured immediately before fission ($n = 52$ fissions). In **g** and **i**, circles indicate individual measurements; line, mean; bounds of box, 25th and 75th percentiles; whiskers, minimum and maximum values; light blue area indicates mean intensity in non-dividing mitochondria (± s.d.). Scale bars, 0.5 μm in **b**, **f**, **h** and 10 μm in **d**. Arrows indicate fission sites. All panels excluding **d** and **e** show data from Cos-7 cells. ***$P < 0.001$. Number of experiments, statistical tests and exact P values are provided in Supplementary Table 1.

from midzone fissions. Similarly, the genetically encoded pH sensor SypHer reported a reduced matrix pH in small daughter mitochondria before fission (Extended Data Fig. 2, Supplementary Video 4). Small peripheral daughter mitochondria containing mito–GFP maintained their intensity; therefore, these results cannot be explained by their reduced volume (Extended Data Fig. 2). Furthermore, the smallest mitochondria derived from midzone fission are similar in size to those from peripheral fissions.

Another indication of mitochondrial dysfunction is ROS accumulation, usually eliminated by anti-oxidative enzymes[15]. ROS levels measured by MitoSOX (Fig. 1h, i) and genetically encoded mito–GRX1–roGFP (Extended Data Fig. 2) were elevated in peripheral daughter mitochondria compared with those in non-dividing mitochondria or daughters from midzone fissions. Cells treated with a 500 nM concentration of the ROS scavenger MitoQ exhibited reduced peripheral fission rates, whereas midzone fission rates were unaffected (Extended Data Fig. 2). Finally, we examined mitochondrial Ca^{2+} levels with the genetically encoded sensors mito–R-GECO1 (Extended Data Fig. 2, Supplementary Video 5) and CEPIA3–mt (Extended Data Fig. 2). Mitochondrial Ca^{2+} has a role in cell survival and death by buffering homeostasis[16]. Ca^{2+} levels increased significantly in small peripheral daughter mitochondria, and mildly in large peripheral daughter mitochondria, compared with midzone or non-dividing mitochondria. Thus, we found no differences in the physiological states of midzone fissions before or after fission, whereas peripheral fission is preceded by increased Ca^{2+} and ROS, and reduced membrane potential and pH.

Distinct positions and distinct fates

As individual mitochondria showed signs of stress and damage upstream of peripheral fission, we hypothesized that it could lead to degradation, whereas midzone fission could serve biogenesis. To test this, we analysed the distribution of mitochondrial DNA (mtDNA) in Cos-7 cells stained with PicoGreen (Fig. 2a, b, Extended Data Fig. 3a). On average, there was no significant difference in the total number of mtDNA foci (nucleoids) between peripherally and centrally dividing mitochondria. However, we observed that 32% of smaller daughter mitochondria from peripheral fissions contained no nucleoids, compared with 3% of those from midzone fissions. Mitochondria lacking mtDNA also had diminished membrane potential compared with those containing mtDNA (Extended Data Fig. 3b). We observed similar results for mitochondrial RNA granules (Extended Data Fig. 3c–e), which are composed of mtRNA and RNA-processing proteins[17]. Daughter mitochondria from midzone fissions contained an elevated number of replicating, TWINKLE-positive nucleoids compared with non-dividing mitochondria, consistent with a proliferative role (Fig. 2c, d, Extended Data Fig. 3f). By contrast, 75% of smaller peripheral daughter mitochondria contained no TWINKLE foci. We then induced mtDNA damage by exposure to ultraviolet (UV) light (Fig. 2e, f) and labelled newly synthesized RNA with bromouridine (BrU). We found that mitochondria had fewer BrU foci after UV treatment, indicating disruption of transcription (Extended Data Fig. 3g). Consistent with their putative degradative role, the prevalence of nucleoids was increased in small peripheral daughter mitochondria (82% compared with 68% without UV irradiation).

We followed daughter mitochondria resulting from peripheral fissions, to discern their fates. Previous studies reported lysosome–mitochondria contacts before fission[18], which we observed in 92% of peripheral fissions, compared with only 13% of midzone fissions (Fig. 2g, h, Supplementary Video 6). At peripheral fission sites, we also observed mitochondria-derived vesicles, which are known to be targeted to late endosomes for degradation[19] (Extended Data Fig. 6c, d). Mitochondria that were undergoing peripheral fission also accumulated YFP–Parkin (Fig. 2i, j). These signatures link peripheral fission with mitophagy, the turnover of mitochondria by PINK1 and Parkin-regulated autophagy[20]. In some cases, we observed the uptake of small daughter mitochondria
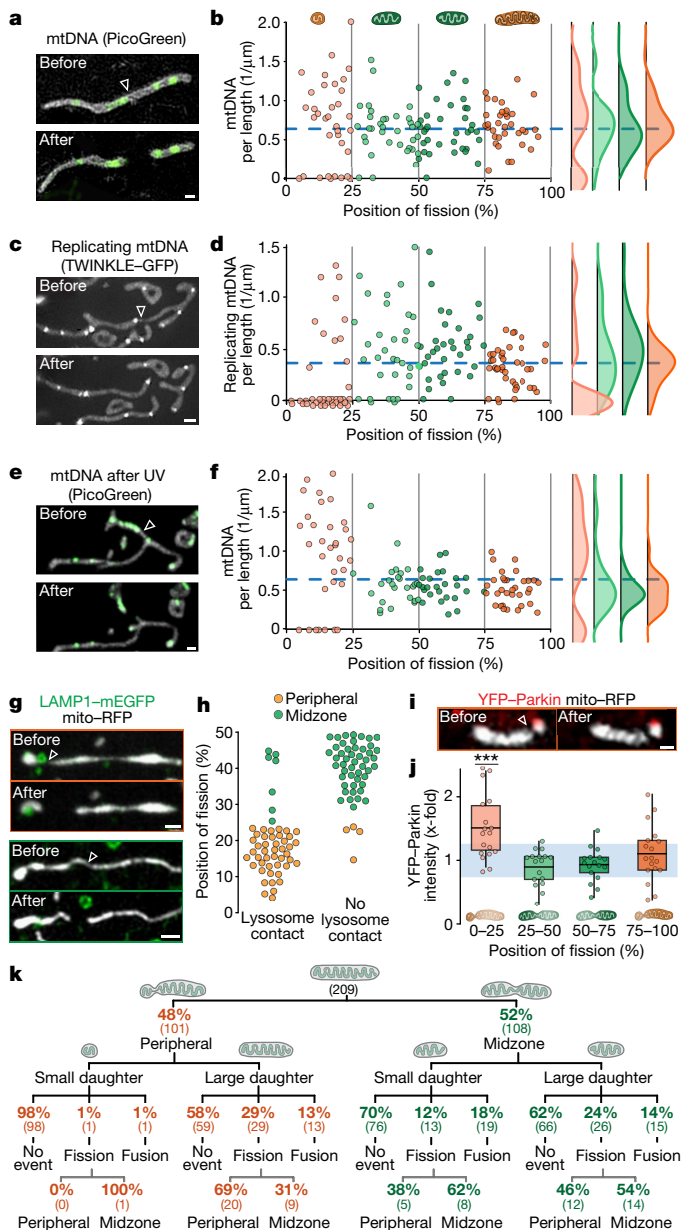
Fig. 2 | Midzone and peripheral fissions differ in mitochondrial DNA content and fates. a, Mitochondria (mito–RFP) and mitochondrial (mt)DNA (PicoGreen, green) before and after fission. **b**, Linear density of nucleoids as a function of fission position, individual data points (left) and violin plots (right) for binned groups (*n* = 78 fissions). **c**, **d**, Replicating nucleoids (TWINKLE–GFP) (**c**) and linear density (**d**), as in **b** (*n* = 74 fissions). **e**, **f**, mtDNA (**e**) and linear density (**f**) after UV irradiation, as in **b** (*n* = 62 fissions). **g**, Mitochondria (mito–RFP, greyscale) and lysosomes (LAMP1–mEGFP, green) before and after peripheral or midzone fission. **h**, Position of fission in divisions contacting lysosomes or not before fission (*n* = 104 fissions). **i**, Mitochondria (mito–RFP, greyscale) and pre-mitophagic marker (YFP–Parkin, red) before and after fission. **j**, Pre-fission YFP–Parkin fold-change in intensity as a function of fission position (*n* = 34). **k**, Schema depicting the fates of daughter mitochondria from peripheral and midzone fissions. Mitochondria tracked for >100 s after fission were included. Numbers in parentheses are total numbers of events. All panels show data from Cos-7 cells, and circles indicate individual measurements. In **b**, **d** and **f**, the blue line represents mean mitochondrial DNA density. In **j**, line, mean, bounds of box, 25th and 75th percentiles; whiskers, minimum and maximum values; light blue area indicates mean intensity in non-dividing mitochondria (± s.d.). Scale bars, 0.5 μm. White arrowheads indicate fission sites. ***P < 0.001. Number of experiments, statistical tests and exact *P* values are provided in Supplementary Table 1.

derived from peripheral fissions by autophagosomes (Extended Data Fig. 3h, Supplementary Video 7). To determine the sequence of events leading to fission, we analysed the timing of changes in mitochondrial physiology (Extended Data Fig. 4) and recruitment of the fission and autophagic machinery. This revealed that a drop in membrane potential, a rise in Ca^{2+} and recruitment of the autophagic machinery all precede peripheral fission. Changes in membrane potential and Ca^{2+} occur even before the inner mitochondrial membrane is notably constricted (Extended Data Fig. 4c), suggesting that compartmentalization occurs before fission.

Previous studies established a paradigm whereby dividing mitochondria either re-fuse with the network or remain isolated and undergo mitophagy[1]. Therefore, we followed the fate of daughter mitochondria after division. We found that, in contrast to other mitochondria, small peripheral daughter mitochondria are excluded from further fusions or divisions in both Cos-7 cells (Fig. 2k) and primary mouse cardiomyocytes (Extended Data Fig. 5a).

Cell context-dependent modulation

To determine whether cells would be able to modulate each fission type independently, in a context-dependent manner (Fig. 3a, b), we subjected Cos-7 cells to metabolic stress by growing them in glucose-free, galactose-supplemented medium. We observed that the rate of peripheral fissions per cell increased, whereas the rate of centrally dividing mitochondria remained constant (Fig. 3a, Extended Data Fig. 5b). A similar trend emerged in response to mtDNA damage induced by UV light. We also tested the effects of increased energy demand and hence oxidative stress on primary mouse cardiomyocytes, by treatment with isoproterenol, a non-selective β-adrenergic receptor agonist that increases contractility and induces hypertrophy. We imaged cells after 48 h of stimulation and found increased rates of peripheral fission compared with non-treated cells, whereas the rate of midzone fission remained constant (Fig. 3b, Extended Data Fig. 5c). By contrast, when cells proliferate, our model predicts an upregulation of midzone fissions. To test this, we treated cardiomyocytes with a microRNA (miR)-199 mimic; we found increased rates of midzone fission, whereas peripheral fission rates remained unchanged (Fig. 3b, Extended Data Fig. 5d). Thus, cellular stress and high energy demands, associated with oxidative damage, increase the rate of peripheral fission, whereas cell proliferation, which requires the biogenesis of new mitochondria, increases the rate of midzone fission.

Distinct molecular machineries

The differences in physiology and fate between mitochondria that are derived from midzone fissions and those derived from peripheral fissions prompted us to investigate the molecular players involved. Previous studies reported that mitochondrial–endoplasmic reticulum (ER) contacts[6], in coordination with actin polymerization[21], define division sites and trigger mtDNA replication upstream of DRP1. All fissions we observed were spontaneous and mediated by DRP1 assembly (Extended Data Fig. 6a, b). We found that midzone fission sites consistently contacted the ER before fission, but most peripheral fission sites did not (Fig. 3c, d, Extended Data Fig. 6h, Supplementary Video 8). In accordance with that observation, immunostaining against PDZD8, a mitochondria–ER tethering protein[22], revealed a higher fluorescence signal at midzone fission sites (Extended Data Fig. 6e, f). This conditional involvement of ER contacts in midzone fissions lends insight to reports that not all fissions engage ER contacts (60–90%)[6,23] or include mtDNA replication (77%)[24]. Similarly, we found that actin consistently polymerized at midzone, but not peripheral fission sites (Fig. 3e, f). Small interfering RNA (siRNA) of INF2, a formin protein that accelerates actin polymerization at the ER[21], led to decreased rates of midzone fission, while having no effect on rates of peripheral fission (Extended Data Figs. 6g, 7a).

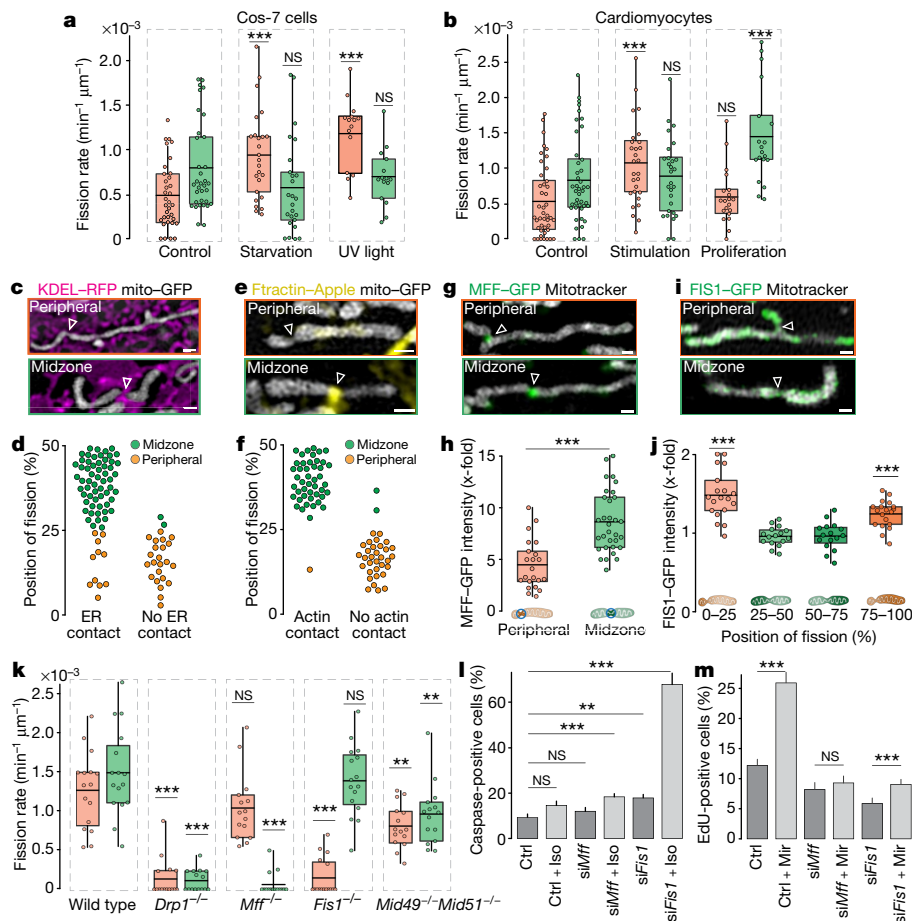**Fig. 3 | Midzone and peripheral fissions are independently regulated by distinct molecular machineries. a**, Peripheral (orange) and midzone (green) fission rates in control, starved or UV-exposed Cos-7 cells ($n \geq 15$ fields of view (FOV) per group). **b**, Fission rates in postnatal mouse cardiomyocytes in control, stimulated or proliferation-induced cells ($n \geq 19$ FOV per group). **c**, SIM of mitochondria (mito–GFP, grey) and endoplasmic reticulum (ER) (KDEL–RFP, magenta) before a peripheral or midzone fission. **d**, Position of fission in mitochondria contacting the ER (left) or not (right) before fission ($n = 93$ fissions) in Cos-7 cells. **e**, SIM of mitochondria (mito–GFP, grey) and actin (Ftractin–Apple, yellow) before peripheral and midzone fissions. **f**, Fission position in mitochondria that accumulate actin (left) or not (right) before fission ($n = 80$ fissions). **g**, SIM of mitochondria (Mitotracker Red, grey) in U2OS cells endogenously expressing MFF–GFP for a peripheral and a midzone fission. **h**, MFF–GFP fold-change in intensity at the fission site of peripheral and midzone divisions ($n = 54$ fissions). **i**, SIM of mitochondria (Mitotracker Red, grey) in U2OS

cells endogenously expressing FIS1–GFP (green) for a peripheral and a midzone fission. **j**, FIS1–GFP fold-change in intensity over the surface of a daughter mitochondrion before fission ($n = 35$ fissions). **k**, Peripheral (orange) and midzone (green) fission rates in wild-type, $Drp1^{-/-}$, $Mff^{-/-}$, $Fis1^{-/-}$ and $Mid49^{-/-}$ $Mid51^{-/-}$ double-knockout mouse embryonic fibroblasts, stained with Mitotracker Green ($n \geq 15$ cells per group). **l**, Percentage of apoptotic (caspase 3/caspase 7-positive) cardiomyocytes ($\pm$ s.e.m.) in control, FIS1- and MFF-depleted cells with or without stimulation with isoproterenol ($n > 29$ FOV per group). **m**, Percentage of proliferating (EdU-positive) cardiomyocytes ($\pm$ s.e.m.) in control, FIS1- and MFF-depleted cells with or without treatment with miR-199 (Mir) ($n \geq 49$ FOV per group). In **a**, **b**, **h**, **j** and **k**, line, mean; bounds of box, 25th and 75th percentiles; whiskers, minimum and maximum values; circles, individual measurements. Number of experiments, statistical tests and exact P values are provided in Supplementary Table 1; NS $P > 0.05$, **$P < 0.01$, ***$P < 0.001$. Scale bars, 0.5 μm. Constriction sites are indicated by white arrowheads.

Several mitochondrial outer membrane proteins (MFF[9], MiD49 and MiD51 (hereafter MiD49/MiD51) (ref. [10]) and FIS1 (ref. [25])) regulate fission, but whether their roles are redundant or distinct remains unclear[11]. To investigate their roles in midzone versus peripheral fissions, we generated U2OS cell lines that express endogenously tagged MFF–GFP or FIS1–GFP. Live-cell structured illumination microscopy revealed stark differences in the distribution of MFF and FIS1. MFF forms bright foci at constrictions that lead to midzone fissions, and foci that were twofold dimmer at peripheral fissions (Fig. 3g, h). By contrast, FIS1 does not show a punctate accumulation, decorating the outer membrane more evenly. However, we observed a significant enrichment of FIS1–GFP on small daughter mitochondria from peripheral divisions (Fig. 3i–j, Extended Data Fig. 6o), consistent with its reported roles in mitophagy[26] and lysosome recruitment[18]. We observed similar distribution patterns of immunolabelled MFF and FIS1 in Cos-7 cells (Extended Data Fig. 6i–l) but did not find differences in accumulation of the DRP adaptors MiD49/MiD51 (Extended Data Fig. 6m, n). To quantify the

distinct roles of MFF, FIS1 and MiD49/MiD51, we measured peripheral and midzone fissions in wild-type and knockout mouse embryonic fibroblast (MEF) lines[11] ($Drp1^{-/-}$, $Mff^{-/-}$, $Fis1^{-/-}$, $Mid49^{-/-}Mid51^{-/-}$ double knockout and $Mff^{-/-}Mid49^{-/-}Mid51^{-/-}$ triple knockout (Fig. 3k, Extended Data Fig. 6p). Although $Drp1^{-/-}$ MEFs show a global inhibition of fission, Mff knockout reduces only midzone fission rates, and conversely, $Fis1$ knockout reduces only peripheral fission rates. We obtained similar results with siRNA-mediated knockdown of $FIS1$ and MFF (Extended Data Figs. 6q, 7b–d). By contrast, cells depleted of MiD49 and MiD51 exhibit a 35% decrease in both peripheral and midzone fission rates, compared with wild-type cells. Thus, MiD49 and MiD51 are engaged in but not required for both types of fission.

To examine the implications of adaptor depletions, we studied their effect on the response of cardiomyocytes to perturbations. We induced contraction for 48 h in cardiomyocytes and subsequently quantified apoptosis in control and FIS1-depleted cells (Fig. 3l, Extended Data Fig. 7e, f). We found that 68% of stimulated cardiomyocytes that lack

FIS1 underwent apoptosis (in contrast to 9–18% in control groups). FIS1 depletion also decreased proliferation rates, even in control conditions, perhaps owing to disrupted mitochondrial quality control, which is linked to cell cycle arrest in cardiomyocytes[27]. Finally, we knocked down *Mff* in cardiomyocytes that were stimulated to proliferate. Although miR-199 increased cell proliferation in the control group, MFF-depleted cell proliferation rates were significantly reduced (Fig. 3m, Extended Data Fig. 7e, f). This further highlights the importance of MFF-mediated midzone fissions for mitochondrial biogenesis during cell proliferation and FIS1-mediated peripheral fission for cell survival under stress conditions.

Discussion

Previous studies revealed that fission underlies both proliferation and degradation of mitochondria[1]. We discovered organelle-level regulation that reconciles this paradox, with the positioning of the fission site as a key morphological signature of the decision to proliferate or degrade. The formation of small daughter mitochondria to sequester damaged components has an advantage: such small mitochondria can be engulfed by autophagosomes and allow the mass of degraded material to be minimized. Our fine spatiotemporal analyses of mitochondrial physiology revealed that most peripheral divisions are preceded by a decrease in membrane potential and proton motive force, and an increase in ROS and Ca^{2+} levels, well before the constriction by DRP1. Although it is remarkable that a gradient forms within one mitochondrion, biological systems frequently use gradients to monitor their geometries[28], and even individual cristae can maintain different membrane potentials[29]. Thus, we speculate that peripheral fissions could use this gradient as a positioning cue, in the absence of extramitochondrial membrane contacts to define the location of the division site. This would explain how cells may regulate peripheral and midzone mitochondrial divisions independently, through intrinsic signals that reflect mitochondrial physiology.

Independent regulation is further supported by our observation that different adaptor proteins mediate peripheral and midzone fissions. Such a paradigm could account for the reported variability and seeming redundancy in the division machinery[30]. MFF accumulates at, and is only required for, midzone fissions, whereas FIS1 is important for regulation of peripheral fission. Weaker accumulation of MFF at poles and peripheral fission sites may be driven by curvature[6]. Initially, FIS1 was proposed to act as a DRP1 adaptor in yeast[31], but later studies in mammalian cells found no direct interactions with DRP1 (ref. [11]). Indeed, we observe a global enrichment of FIS1 on the outer membrane of small, peripherally dividing mitochondria, instead of foci. Therefore, we propose that FIS1 does not act as a DRP1 adaptor, but instead regulates peripheral fission through the recruitment of lysosomes, consistent with findings that FIS1 recruits the lysosome–mitochondria tethering molecule TBC1D15 (ref. [18]).

The existence of two mechanistically and functionally distinct types of fission has implications in the context of pathology. Excessive fission rates are a hallmark of diverse diseases[4,32], and pharmacological inhibition of fission has been proposed as a potential therapy[33]. Other therapeutic approaches have aimed to stimulate mitochondrial biogenesis[34]. However, our model suggests that if under pathological conditions only one type of fission is dysregulated, treatment with global inhibitors may further disrupt cell homeostasis. Therefore, our findings indicate the potential for more rational and specific therapeutic targets.

Online content

Any methods, additional references, Nature Research reporting summaries, source data, extended data, supplementary information, acknowledgements, peer review information; details of author contributions and competing interests; and statements of data and code availability are available at https://doi.org/10.1038/s41586-021-03510-6.

1. Twig, G. et al. Fission and selective fusion govern mitochondrial segregation and elimination by autophagy. *EMBO J.* **27**, 433–446 (2008).
2. Rambold, A. S., Kostelecky, B., Elia, N. & Lippincott-Schwartz, J. Tubular network formation protects mitochondria from autophagosomal degradation during nutrient starvation. *Proc. Natl Acad. Sci. USA* **108**, 10190–10195 (2011).
3. Song, M., Franco, A., Fleischer, J. A., Zhang, L. & Dorn, G. W., II. Abrogating mitochondrial dynamics in mouse hearts accelerates mitochondrial senescence. *Cell Metab.* **26**, 872–883 (2017).
4. Wang, W. et al. Parkinson's disease-associated mutant VPS35 causes mitochondrial dysfunction by recycling DLP1 complexes. *Nat. Med.* **22**, 54–63 (2016).
5. Ma, J.-T. et al. Effects of dynamin-related protein 1 regulated mitochondrial dynamic changes on invasion and metastasis of lung cancer cells. *J. Cancer* **10**, 4045–4053 (2019).
6. Friedman, J. R. et al. ER tubules mark sites of mitochondrial division. *Science* **334**, 358–362 (2011).
7. Ji, W. K., Hatch, A. L., Merrill, R. A., Strack, S. & Higgs, H. N. Actin filaments target the oligomeric maturation of the dynamin GTPase Drp1 to mitochondrial fission sites. *eLife* **4**, e11553 (2015).
8. Smirnova, E., Griparic, L., Shurland, D. L. & van der Bliek, A. M. Dynamin-related protein Drp1 is required for mitochondrial division in mammalian cells. *Mol. Biol. Cell* **12**, 2245–2256 (2001).
9. Gandre-Babbe, S. & van der Bliek, A. M. The novel tail-anchored membrane protein Mff controls mitochondrial and peroxisomal fission in mammalian cells. *Mol. Biol. Cell* **19**, 2402–2412 (2008).
10. Palmer, C. S. et al. MiD49 and MiD51, new components of the mitochondrial fission machinery. *EMBO Rep.* **12**, 565–573 (2011).
11. Osellame, L. D. et al. Cooperative and independent roles of the Drp1 adaptors Mff, MiD49 and MiD51 in mitochondrial fission. *J. Cell Sci.* **129**, 2170–2181 (2016).
12. Fröhlich, C. et al. Structural insights into oligomerization and mitochondrial remodelling of dynamin 1-like protein. *EMBO J.* **32**, 1280–1292 (2013).
13. Burman, J. L. et al. Mitochondrial fission facilitates the selective mitophagy of protein aggregates. *J. Cell Biol.* **216**, 3231–3247 (2017).
14. Ashrafi, G. & Schwarz, T. L. The pathways of mitophagy for quality control and clearance of mitochondria. *Cell Death Differ.* **20**, 31–42 (2013).
15. Sturtz, L. A., Diekert, K., Jensen, L. T., Lill, R. & Culotta, V. C. A fraction of yeast Cu,Zn-superoxide dismutase and its metallochaperone, CCS, localize to the intermembrane space of mitochondria. A physiological role for SOD1 in guarding against mitochondrial oxidative damage. *J. Biol. Chem.* **276**, 38084–38089 (2001).
16. Mallilankaraman, K. et al. MICU1 is an essential gatekeeper for MCU-mediated mitochondrial Ca^{2+} uptake that regulates cell survival. *Cell* **151**, 630–644 (2012).
17. Jourdain, A. A. et al. GRSF1 regulates RNA processing in mitochondrial RNA granules. *Cell Metab.* **17**, 399–410 (2013).
18. Wong, Y. C., Ysselstein, D. & Krainc, D. Mitochondria-lysosome contacts regulate mitochondrial fission via RAB7 GTP hydrolysis. *Nature* **554**, 382–386 (2018).
19. Soubannier, V., Rippstein, P., Kaufman, B. A., Shoubridge, E. A. & McBride, H. M. Reconstitution of mitochondria derived vesicle formation demonstrates selective enrichment of oxidized cargo. *PLoS One* **7**, e52830 (2012).
20. Pickles, S., Vigié, P. & Youle, R. J. Mitophagy and quality control mechanisms in mitochondrial maintenance. *Curr. Biol.* **28**, R170–R185 (2018).
21. Korobova, F., Ramabhadran, V. & Higgs, H. N. An actin-dependent step in mitochondrial fission mediated by the ER-associated formin INF2. *Science* **339**, 464–467 (2013).
22. Hirabayashi, Y. et al. ER-mitochondria tethering by PDZD8 regulates Ca^{2+} dynamics in mammalian neurons. *Science* **358**, 623–630 (2017).
23. Murley, A. et al. ER-associated mitochondrial division links the distribution of mitochondria and mitochondrial DNA in yeast. *eLife* **2**, e00422 (2013).
24. Lewis, S. C., Uchiyama, L. F. & Nunnari, J. ER-mitochondria contacts couple mtDNA synthesis with mitochondrial division in human cells. *Science* **353**, aaf5549 (2016).
25. Yu, R., Jin, S.-B., Lendahl, U., Nistér, M. & Zhao, J. Human Fis1 regulates mitochondrial dynamics through inhibition of the fusion machinery. *EMBO J.* **38**, e99748 (2019).
26. Xian, H., Yang, Q., Xiao, L., Shen, H.-M. & Liou, Y.-C. STX17 dynamically regulated by Fis1 induces mitophagy via hierarchical macroautophagic mechanism. *Nat. Commun.* **10**, 2059 (2019).
27. Kimura, W. et al. Redox signaling in cardiac renewal. *Antioxid. Redox Signal.* **21**, 1660–1673 (2014).
28. Chang, F. & Minc, N. Electrochemical control of cell and tissue polarity. *Annu. Rev. Cell Dev. Biol.* **30**, 317–336 (2014).
29. Wolf, D. M. et al. Individual cristae within the same mitochondrion display different membrane potentials and are functionally independent. *EMBO J.* **38**, e101056 (2019).
30. Koirala, S. et al. Interchangeable adaptors regulate mitochondrial dynamin assembly for membrane scission. *Proc. Natl Acad. Sci. USA* **110**, E1342–E1351 (2013).
31. Mozdy, A. D., McCaffery, J. M. & Shaw, J. M. Dnm1p GTPase-mediated mitochondrial fission is a multi-step process requiring the novel integral membrane component Fis1p. *J. Cell Biol.* **151**, 367–380 (2000).
32. Song, W. et al. Mutant huntingtin binds the mitochondrial fission GTPase dynamin-related protein-1 and increases its enzymatic activity. *Nat. Med.* **17**, 377–382 (2011).
33. Guo, X. et al. Inhibition of mitochondrial fragmentation diminishes Huntington's disease-associated neurodegeneration. *J. Clin. Invest.* **123**, 5371–5388 (2013).
34. Zamora, M., Pardo, R. & Villena, J. A. Pharmacological induction of mitochondrial biogenesis as a therapeutic strategy for the treatment of type 2 diabetes. *Biochem. Pharmacol.* **98**, 16–28 (2015).

Article

Methods

No statistical methods were used to predetermine sample size. For studies involving multiple experimental conditions, studies were performed on cells originated from the same cell line batch and randomly assigned to experimental conditions.

Plasmids and reagents

Mito–GFP (Cox-8 presequence) was a gift from H. Shroff (NIH, Bethesda), mCherry–DRP1 and BFP–KDEL were gifts from G. Voeltz (Addgene, plasmid no. 49152 and no. 49150)[6], SypHer mt was a gift from N. Demaurex (Addgene plasmid no. 48251)[35], pLPCX mito–GRX1–roGFP2 was a gift from T. Dick (Addgene plasmid no. 64977)[36], pCMV CEPIA3–mt was a gift from M. Iino (Addgene plasmid no. 58219)[37], LAMP1–mEGFP was a gift from R. Vale (Addgene plasmid no. 16290)[38], YFP–Parkin was a gift from R. Youle (Addgene plasmid no. 23955)[39] and EGFP–LC3 was a gift from K. Kirkegaard (Addgene plasmid no. 11546)[40], CMV-mito–R-GECO1 was a gift from R. Campbell (Addgene plasmid no. 46021)[41]. FASTKD2–EGFP and TWINKLE–EGFP[42] were gifts from J.-C. Martinou. Ftractin-Apple was a gift from H. N. Higgs (Dartmouth College, Hanover), mito–tagRFP was amplified from mito–GFP. Wild-type, $Drp1^{-/-}$, $Mff^{-/-}$, $Fis1^{-/-}$, $Mid49^{-/-}Mid51^{-/-}$ double knockout, $Mff^{-/-}Mid49^{-/-}Mid51^{-/-}$ triple knockout mouse embryonic fibroblasts were a gift from M. Ryan and have previously been described[11].

The stable FASTKD2–EGFP cell line was recently described[43]. In brief, co-transfection of human embryonic kidney 293T (HEK293T) cells (ATCC CRL-11268) with pWPT_FASTKD2–EGFP and packaging plasmids pMD2.G and psPAX2 was achieved using calcium phosphate precipitation. Medium containing virus was collected 48 h after transfection and filtered using membranes with a pore size of 0.45 µm. The viral supernatant and polybrene were added to 70% confluent recipient cells. Fluorescence-activated cell sorting (FACS) was performed to select for cells expressing GFP.

Oligonucleotides for siRNA were made by Microsynth to knock down *MFF* (sense strand 5′-CGC UGA CCU GGA ACA AGG A-dTdT-3′), *FIS1* (sense strand 5′-CGA GCU GGU GUC UGU GGA G-dTdT-3′) and *INF2* (sense strand 5′-GCA GUA CCG CUU CAG CAU UGU CAU T-3′ and 5′-GGA UCA ACC UGG AGA UCA UCC GCT T-3′). siRNA transfection was performed using Lipofectamine RNAi Max (Invitrogen) and cells were imaged 72 h after transfection.

The following reagents were also used: Mitotracker Green (ThermoFisher M7514), Mitotracker Red FM (ThermoFisher M22425), tetramethylrhodamine ethyl ester perchlorate (Sigma, 87917), MitoSOX Red Mitochondrial Superoxide Indicator (Thermo Fisher M36008), Mitoquinol 98% (Adipogen SA CAY-89950-10), Quant-iT PicoGreen (Life Technologies P7581), CellEvent Caspase-3/7 (Life Technologies C10723), FIS1 polyclonal antibody (Proteintech 109561-AP), MFF (C2orf33) polyclonal antibody (Life Technologies PA567357), PDZD8 polyclonal antibody (Life Technologies PA553368), MiD49 (SMCR7) polyclonal antibody (Life Technologies, PA559950), TOM20 mouse monoclonal antibody (Santa Cruz sc-17764) and Alexa fluorophore-conjugated secondary antibodies from Life Technologies.

Generation of knock-in U2OS cells

CRISPR–Cas9-mediated knock-in of EGFP into the *MFF* locus directly upstream of the start codon was performed using a plasmid encoding EGFP2 flanked by 729 bp of upstream and 723 bp of downstream homologous DNA sequence cloned into pEX-A258 to create plasmid pTW344 (pEX-A258–EGFP_hMFF_Template KI). Two pairs of single guide DNA (sgDNA) targeting *MFF* (sgDNA1: forward 5′- aaacAGTGATG TGTCACTGCTTGTC-3′ and reverse 5′ CACCGACAAGCAG TGACACATCACT-3′, sgDNA2: forward 5′- CACCGCATTTAAATACAG TAAATAC and reverse 5′- aaacGTATTTACTGTATTTAAATGC-3′) were cloned into pSpCas9n(BB)-2A-Puro (PX462) V2.0 (a gift from F. Zhang (Addgene plasmid no. 62987))[44].

CRISPR–Cas9-mediated knock-in of EGFP into the *FIS1* locus directly upstream of the start codon was performed using a plasmid encoding EGFP2 flanked by 721 bp of upstream and 624 bp of downstream homologous DNA sequence cloned into pEX-A258 to create plasmid pTW343 (pEX-A258–EGFP_hFIS1_Template KI). Two pairs of sgDNA targeting *FIS1* (sgDNA1: forward 5′- CACCGCTGAACGAGCTGGTGTCTG-3′ and reverse 5′ aaacCAGACACCAGCTCGTTCAGC-3′, sgDNA2: forward 5′- CACCGCTCGTTCAGCACGGCCTCCA and reverse 5′- aaacTGGAGGCCGTGCTGAACGAGC-3′) were cloned into pSpCas9n(BB)-2A-Puro (PX462) V2.0 (a gift from F. Zhang (Addgene plasmid no. 62987)). To knock in *EGFP* into either the *MFF* or the *FIS1* loci, U2OS cells were co-transfected with pSpCas9n(BB)-2A-Puro (PX462) V2.0 constructs carrying the appropriate sgDNA sequences and linearized template plasmids (pTW343 for hMFF and pTW344 for hFIS1) using Lipofectamine 2000. GFP-positive cells were individually isolated 24 h after transfection by FACS. Clones were expanded and were validated by PCR genotyping of genomic DNA and fluorescent imaging.

Cell culture and transfection

Cells were grown either in Dulbecco's modified Eagle's medium (DMEM) supplemented with 10% fetal bovine serum and maintained in culture for a maximum of 20 passages or in galactose-supplemented medium[45]. Cells were plated on 25-mm glass coverslips (Menzel, no. 1.5) 10–24 h before transfection at 1×10^5 cells ml^{-1}. Plasmid transfections were performed with 1.5 µl of Lipofectamine 2000 (Invitrogen) per 100 µl of Opti-MEM medium (Invitrogen). The following amounts of DNA were transfected per ml: 150 ng of mito–GFP, 250 ng of mito–tagRFP, 100 ng of mCherry–DRP1, 300 ng of TOM20–RFP, 400 ng of mito–SypHer, 400 ng of mito–GRX1–roGFP2, 150 ng of mito-R-GECO1, 400 ng of CEPIA3–mt, 350 ng of KDEL–RFP, 250 ng of LAMP1–mEGFP, 350 ng of EGFP–LC3, 400 ng of YFP–Parkin and 200 ng of TWINKLE–GFP. Cells were imaged the next day.

All cell lines were routinely tested for *Mycoplasma* contamination and discarded if positive. Cos-7 cells (ECACC 87021302) and U2OS cells (ECACC 92022711) were obtained from ECACC, and HEK293T cells (ATCC CRL-11268) were obtained from ATCC. ECACC and ATCC use STR profiling for authentication.

Primary mouse cardiomyocyte culture

Cardiac myocytes were prepared from ventricles of P1 neonatal mice using Pierce Cardiomyocyte Isolation Kit (Life Technologies 88281) following the manufacturer's instructions. After digestion, the adherent non-myocyte cells were removed by pre-plating in 10-cm tissue culture plates for 45 min. The non-adherent cardiomyocytes were seeded in complete cardiomyocyte plating medium supplemented with 10% fetal calf serum (FCS) and antibiotics at a density of $4–5 \times 10^5$ cells/well on poly-L-lysine (Sigma P-7890) and gelatin (Sigma G9891)-coated coverslips in six-well plates. To stimulate contraction, 24 h after plating the cardiomyocytes were fed with fresh medium supplemented with 2% FCS and with 10^{-5} M isoproterenol (Sigma I-2760). To induce proliferation, cardiomyocytes were transfected with 50 nM miR-199 mimic[46] (Pharmacon, miRIDIAN Mimic Has-miR-199a-3p; C300535-05) using Lipofectamine RNAi-Max following the manufacturer's instructions (Life Technologies, 13778). Cardiomyocytes were observed 48 h after treatment or transfection.

Western blotting

For immunoblots 48–72 h after siRNA transfection (Supplementary Fig. 1), Cos-7 cells were lysed in radioimmunoprecipitation (RIPA) buffer (Sigma) supplemented with fresh proteases inhibitors (Sigma Aldrich 11836170001) on ice for 30 min. A centrifugation at 16,000g for 10 min at 4 °C was performed to remove the insoluble material. Protein concentrations were determined using a Pierce BCA protein assay kit (Life Technologies, 23227) and equal amounts of protein were analysed by self-casted 7.5% or 15% SDS–PAGE (30–50 µg of protein

per lane). For immunoblotting, proteins were transferred to nitrocellulose membranes (BioRad) electrophoretically and incubated with the specified primary antibodies (see above), diluted in 5% non-fat dry milk in Tris-buffered saline with Tween 20 (TBST). The blots were further incubated with anti-rabbit or anti-mouse horseradish peroxidase (HRP)-conjugated secondary antibodies (GE Healthcare) and visualized using ECL (GE Healthcare). Where required, images of western blotting were treated for contrast enhancement, and densitometric analyses were performed using ImageJ.

Primary antibodies used for western blot
The following primary antibodies were used for western blots: anti-FIS1 (LuBioScience GmbH, 10956-1-AP, diluted 1:2,000), anti-MFF (Life Technologies, PA5-52765, diluted 1:500–1:1,000), anti-INF2 (Sigma-Aldrich HPA000724, diluted 1:2,000), anti-α-tubulin (Santa Cruz sc-5286, diluted 1:2,000).

RT–PCR
Total RNA was extracted from neonatal cardiomyocytes 48 h after transfection using the miRNeasy Mini Kit (Qiagen, no. 1038703). An optional step of DNase (Qiagen no. 79254) digestion was performed following the manufacturer's protocol. cDNA was synthesized from 1 µg of total RNA using the PrimeScript RT–PCR Kit (Takara no. RR014B) and Syber Green qRT–PCR was performed on QuantStudio 12K (Life Technologies) using the Power SYBR Green PCR Master Mix (Applied Biosystems, no. 4367659). For SYBR Green qRT–PCR, 4 µl of cDNA (25 ng µl^{-1}) were mixed with 5 µl of Power SYBR Green PCR Master Mix, 0.5 µl of forward primer (5 µM) and 0.5 µl of reverse primer (5 µM). The cDNA mix was incubated 2 min at 50 °C followed by a denaturation step of 2 min at 95 °C and an amplification step of 40 cycles at 95 °C for 15 s and at 60 °C for 45 s.

The following primers were used: *Fis1* forward primer 5′-CCGGC TCAAGGAATATGAAA-3′; *Fis1* reverse primer 5′-ACAGCCAGTCCAA TGAGTCC-3′; *Mff* forward primer 5′-AGTGTGATAATGCAAGTCCCAGA-3′; *Mff* reverse primer 5′-GAGTGGACTGGATAAGGTCAAGA-3′; *Gapdh* forward primer 5′-TGCACCACCAACTGCTTAGC-3′; and *Gapdh* reverse primer 5′-GGCATGGACTGTGGTCATGAG-3′.

Live-cell treatments
TMRE. Cells were incubated with 500 nM TMRE for 10 min followed by rinsing in phosphate-buffered saline (PBS).

Mitotracker. Cells were incubated in 500 nM Mitotracker for 5 min followed by rinsing in PBS.

PicoGreen. To image mtDNA, cells were stained with PicoGreen diluted 1:500 for 20 min.

MitoSOX. Cells were incubated with 5 µM MitoSOX for 2–4 h before imaging.

MitoQ. Cells were incubated with 500 nM MitoQ[47] for 30–45 min prior and during imaging following the manufacturer's instructions, and fresh aliquots were made every day.

BrU tagging of RNA
Cos-7 cells were incubated with 5 mM 5-bromouridine (BrU) in complete culture medium for 1 h before fixation, as described previously[43]. BrU was stored at −20 °C, and heated and vortexed before use. Samples were immunolabelled with anti-bromodeoxyuridine (BrdU) (Roche 11170376001; 1:250 to 1:500 dilution) to visualize BrU signal.

SIM imaging
Single and dual-colour SIM imaging was performed on a 3D NSIM Nikon inverted fluorescence microscope (Eclipse Ti; Nikon) equipped with an electron charge-coupled device camera (iXon3 897; Andor Technologies). The microscope was equipped with a 100× 1.49 NA oil immersion objective (CFI Apochromat TIRF 100×C Oil; Nikon). Live-cell imaging was performed at 37 °C using a 488-nm and a 561-nm laser. Acquisition settings were adapted to yield the best image quality with minimal photobleaching (laser power 0.5–15%, exposure time 30–100 ms). Images were captured using NIS elements software (Nikon) at temporal resolution of 1 s for single-colour and 6–8 s for dual-colour imaging. Imaging was performed at 37 °C in pre-warmed Leibovitz medium. Each sample was imaged for a maximum of 90 min.

Instant SIM
Single and dual colour iSIM imaging was performed on a custom-built microscope set-up as previously described[48,49]. Fluorescence was collected with a 1.49 NA oil immersion objective (APONXOTIRF; Olympus), with 488-nm and 561-nm excitation lasers and an sCMOS camera (PrimeBSI, 01-PRIME-BSI-R-M-16-C; Photometric). Images were captured at temporal resolution of 0.5–5 s for both channels. All imaging was performed at 37 °C in Leibovitz medium. Raw iSIM images were subsequently deconvolved using the Lucy-Richardson deconvolution algorithm[50] provided by Hari Shroff implemented in MATLAB and were run for 40 iterations.

Confocal imaging
Ratiometric imaging of mito–GRX1–roGFP was performed on an inverted microscope (DMI 6000; Leica) equipped with hybrid photon counting detectors (HyD; Leica). The sample was excited sequentially frame by frame at 408 nm and 488 nm with the detection set to 500–535 nm. Fluorescence was collected through a 63× 1.40 NA oil immersion objective (HC PL APO 63×/1.40 Oil CS2; Leica). Images were captured using the LAS X software (Leica). All imaging was performed at 37 °C in pre-warmed Leibovitz medium for maximum 90 min per sample.

For confocal microscopy of fixed BrU samples the imaging was performed using a Leica TCS SP8 inverted microscope equipped with 405-, 488-, 552- and 638-nm lasers and a Plan-Apochromat oil objective (×63, NA 1.4). The Lightning mode (Leica) was used to generate deconvolved images. Microscope acquisitions were controlled by LAS X (v. 3.5.2) software from Leica.

CLEM and caspase 3/caspase 7 samples were imaged on a Zeiss LSM 700 inverted confocal microscope equipped with a Plan-Apochromat oil objective (×63, NA 1.40) and 488-nm and 555-nm solid-state lasers and three photomultipliers. Acquisitions were controlled by the Zeiss Zen (v. 6.0.0) software.

Immunofluorescence
Cells were seeded on glass coverslips and grown to a confluence of ~80%. Fixation of cultured cells was performed in cold 4% paraformaldehyde (PFA) in PBS for 20 min, then cells were washed 3× in PBS. Subsequently, cells were incubated with 0.3% Triton X-100 and 1% pre-immune goat serum for 30 min. The same buffer was used to incubate cells with the specified primary antibody (see above) overnight at 4 °C. After washing in PBS, cells were incubated with the appropriate secondary antibody for 1 h and rinsed in PBS before imaging.

Immunohistochemistry on cardiomyocytes
Cardiomyocytes (CMs) (P1) were transfected with 25 nM si*Fis1* or si*Mff* for 6 h and then transfected with 50 nM miR-199 mimic for 48 h. EdU was added in fresh medium after 56 h and kept for the last 18 h. Cells were then fixed for 10 min in in 4% PFA in PBS and permeabilized with 0.3% Triton X-100 in PBS. After blocking (PBS containing 0.001% Triton X-100, 1% bovine serum albumin and 1% FCS), cells were incubated overnight at 4 °C with anti-troponin I (1:500). The day after, cells were washed 3× and incubated 1 h at room temperature in the dark with the secondary-conjugated antibody diluted 1:500 (488 goat anti-rabbit A11008; Life Technologies). EdU has been labelled and detected using

Article

a Click-iT EdU Alexa Fluor 594 Imaging Kit (Invitrogen C10339). Nuclei were stained with DAPI (Invitrogen).

Correlated confocal and transmission electron microscopy
Cells were seeded on gridded coverslips (MatTek, P35-1.5-14-CGRD-D) and grown to 50–60% confluence. Cells were fixed at room temperature for 1 h in freshly prepared fixative (2% PFA, 1% glutaraldehyde in PBS 0.1 M, pH 7.4), followed by 10× washing in PBS. Samples were imaged by confocal microscopy on the same day and z-stacks were acquired of whole cells, the pinhole was closed to 0.5 AU and pixel size reduced to 50–100 nm in xy and 100–150 nm in z. Samples were stored overnight, in PBS at 4 °C. They were then stained with osmium and potassium ferrocyanide, followed by osmium alone, each with cacodylate buffer. They were finally stained with 1% uranyl acetate, then washed in water, dehydrated through 15 increasing concentrations of alcohol and infiltrated with Epon resin. This was polymerized over night at 65 °C. Ultra-thin serial sections were then cut of the cell of interest, and the sections were collected on single slot copper grids with a formvar support membrane. Images were recorded in a transmission electron microscope operating at 80 kV (FEI Company, Tecnai Spirit).

Image analysis
All image analysis was performed with the open-source ImageJ/Fiji[51,52] (including Weka Segmentation, EMBL bleach correction plugins). Mitochondrial fissions were defined as events in which a single mitochondrion divided into two independently moving daughter mitochondria in live cells and in fixed cells when a (DRP1-positive) constriction site showed a diameter of <180 nm, measured via FWHM across the constriction. For representation purpose, a 1-pixel Gaussian filter was used and some videos were corrected for bleaching.

Relative position of constriction site.
The positioning of constriction site was measured manually by drawing a line along the length axis of the mitochondrion in the frame before fission. For branched mitochondria (-13% of the mitochondrial population), the lengths of individual branches were summed.

Relative fluorescence intensity.
Intensity measurements of biosensors were analysed by measuring mean fluorescence intensity on each side of the constriction and in single daughter mitochondria after fission (ROI defined by using Otsu thresholding) on SIM images and subtracting the cytosolic background. For normalization, the mean fluorescence intensity was measured in three non-dividing mitochondria within the same FOV at the same time point. For fixed samples (anti-PDZD8, anti-MFF, anti-FIS1, anti-MiD49), the mean intensity was measured in a 500-nm circle placed at the constriction site and normalized over the fluorescent signal along the non-constricted part of the mitochondrion. For measuring DRP1, LAMP1–mEGFP, MFF–GFP and FIS1–GFP intensities, a 500-nm circle was placed at the constriction site and normalized over the intensity of at a 500-nm circle placed on a non-constricted part of the same mitochondrion.

Fission rate.
To measure the fission rate, the total mitochondrial volume was calculated using trainable Weka segmentation (Fiji plugin) followed by binarization of the image. The total mitochondrial length was calculated using the total area in the binarized image divided by the mean mitochondrial diameter. Fission rates were indicated as number of fissions occurring per micrometre length of mitochondrion, per min.

ER or actin contacts.
Contacts between mitochondria and ER or actin were measured by placing a line along the length axis of the mitochondrion crossing the constriction site and measuring the intensity profile for both channels. A contact site was defined, if the two signals cross at the constriction site (ER signal increases at least 2× over background) for at least three consecutive frames before fission.

Lysosome–mitochondria contact.
A contact between mitochondria and lysosome was categorized as close proximity (<500 nm) between lysosomes and the mitochondrial constriction site for at least three consecutive frames before fission.

BrU quantification.
Individual cells were selected manually, using Fiji's rectangular selection tool. Three consecutive slices to focus at the bottom of the cell were then chosen upon inspection and foci were detected automatically in both BrU and FASTKD2 channels using a fixed threshold. Foci that occurred in both channels were then counted as relevant mitochondrial RNA-transcription granules, whereas nuclear transcription, for instance, was excluded from the analysis. Multiple thresholds were tried, where 150 a.u. (a.u.= grey value from a range 0–255) provided the most sensible results in control cells and are represented in Extended Data Fig. 3g, although all other data are provided in the source data files and followed the same trend. The same pipeline was applied to both control and UV-treated samples.

Animal experiments
Mice were housed in a 12-h light/12-h dark cycle at a temperature of 23 °C with 40–60% humidity. All animal experiments were approved by the Government Veterinary Office (Lausanne, Switzerland) and performed according to the University of Lausanne Medical School institutional guidelines.

Statistics and reproducibility
Sample sizes were determined on the basis of previous experience in previous experiments. All statistics were performed using OriginPro software. First, datasets were tested for normal distribution using D'Agostino–Pearson normality test (significance value of 0.05). If a dataset failed this test, a non-parametric test was chosen to compare significance of means between groups (Mann–Whitney test for two samples). For normally distributed datasets, a two-sample t-test was chosen to compare two samples. For a detailed description of statistical tests used and exact P values, please see Supplementary Table 1. Critical comparative datasets (FIS1 and MFF datasets, DRP1 intensity analysis, ER analysis) were partially re-analysed or analysed with an automated analysis pipeline to exclude observer bias. P values <0.05 were considered to be significant and indicated by *; P values <0.01 were indicated by ** and <0.001 by ***.

Reporting summary
Further information on research design is available in the Nature Research Reporting Summary linked to this paper.

Data availability
All imaging as well as numerical data relevant to this study are publicly available on the online repository Zenodo (https://doi.org/10.5281/zenodo.3550643). The data are organized according to their appearance in the main figures and Extended Data figures. The unprocessed western blot gels are provided in Supplementary Fig. 1. Plasmids and cell lines are available from the corresponding authors on request. Source data are provided with this paper.

Code availability
The custom-written Fiji-macro script for BrU quantification is available at https://github.com/TimoHenry/MitochondrialRNAgranules and the custom written Fiji-macro for caspase staining is available at https://github.com/jutziw/mitochondrial_division.

35. Poburko, D., Santo-Domingo, J. & Demaurex, N. Dynamic regulation of the mitochondrial proton gradient during cytosolic calcium elevations. *J. Biol. Chem.* **286**, 11672–11684 (2011).

36. Gutscher, M. et al. Real-time imaging of the intracellular glutathione redox potential. *Nat. Methods* **5**, 553–559 (2008).

37. Suzuki, J. et al. Imaging intraorganellar Ca^{2+} at subcellular resolution using CEPIA. *Nat. Commun.* **5**, 4153 (2014).

38. Minin, A. A. et al. Regulation of mitochondria distribution by RhoA and formins. *J. Cell Sci.* **119**, 659–670 (2006).

39. Narendra, D., Tanaka, A., Suen, D.-F. & Youle, R. J. Parkin is recruited selectively to impaired mitochondria and promotes their autophagy. *J. Cell Biol.* **183**, 795–803 (2008).

40. Jackson, W. T. et al. Subversion of cellular autophagosomal machinery by RNA viruses. *PLoS Biol.* **3**, e156 (2005).

41. Wu, J. et al. Improved orange and red Ca^{2+} indicators and photophysical considerations for optogenetic applications. *ACS Chem. Neurosci.* **4**, 963–972 (2013).

42. Spelbrink, J. N. et al. Human mitochondrial DNA deletions associated with mutations in the gene encoding Twinkle, a phage T7 gene 4-like protein localized in mitochondria. *Nat. Genet.* **28**, 223–231 (2001).

43. Rey, T. et al. Mitochondrial RNA granules are fluid condensates positioned by membrane dynamics. *Nat. Cell Biol.* **22**, 1180–1186 (2020).

44. Ran, F. A. et al. Genome engineering using the CRISPR–Cas9 system. *Nat. Protocols* **8**, 2281–2308 (2013).

45. Marroquin, L. D., Hynes, J., Dykens, J. A., Jamieson, J. D. & Will, Y. Circumventing the Crabtree effect: replacing media glucose with galactose increases susceptibility of HepG2 cells to mitochondrial toxicants. *Toxicol. Sci.* **97**, 539–547 (2007).

46. Eulalio, A. et al. Functional screening identifies miRNAs inducing cardiac regeneration. *Nature* **492**, 376–381 (2012).

47. Kelso, G. F. et al. Selective targeting of a redox-active ubiquinone to mitochondria within cells: antioxidant and antiapoptotic properties. *J. Biol. Chem.* **276**, 4588–4596 (2001).

48. York, A. G. et al. Instant super-resolution imaging in live cells and embryos via analog image processing. *Nat. Methods* **10**, 1122–1126 (2013).

49. Mahecic, D. et al. Homogeneous multifocal excitation for high-throughput super-resolution imaging. *Nat. Methods* **17**, 726–733 (2020).

50. Holmes, T. J. & Liu, Y. H. Richardson-Lucy/maximum likelihood image restoration algorithm for fluorescence microscopy: further testing. *Appl. Opt.* **28**, 4930–4938 (1989).

51. Schindelin, J. et al. Fiji: an open-source platform for biological-image analysis. *Nat. Methods* **9**, 676–682 (2012).

52. Schneider, C. A., Rasband, W. S. & Eliceiri, K. W. NIH Image to ImageJ: 25 years of image analysis. *Nat. Methods* **9**, 671–675 (2012).

Author contributions T.K. and S.M. conceived the project and designed experiments. T.K. performed imaging experiments and analysis. T.R. performed the TWINKLE, FASTKD2, BrU and MitoSOX imaging and contributed to the analysis. T.K. and J.W. performed the caspase, DRP1 and LC3 imaging. D.M. developed and adjusted the iSIM set-up. T.K., T.R. and D.M. performed the transmission electron microscopy (TEM) experiments. S.Z. performed the western blots. F.P.R., M.N. and T.P. designed and performed culturing of mouse cardiomyocytes and the proliferation assay. T.W., S.Z. and H.P.L. designed and cloned the CRISPR–Cas9 transgenic lines. T.K. and S.M. designed figures and wrote the manuscript, with input from all authors.

**Competing interests** The authors declare no competing interests.

Additional information
Supplementary information The online version contains supplementary material available at https://doi.org/10.1038/s41586-021-03510-6.
Correspondence and requests for materials should be addressed to T.K. or S.M.
**Peer review information** *Nature* thanks Henry Higgs and the other, anonymous, reviewer(s) for their contribution to the peer review of this work.
Reprints and permissions information is available at http://www.nature.com/reprints.
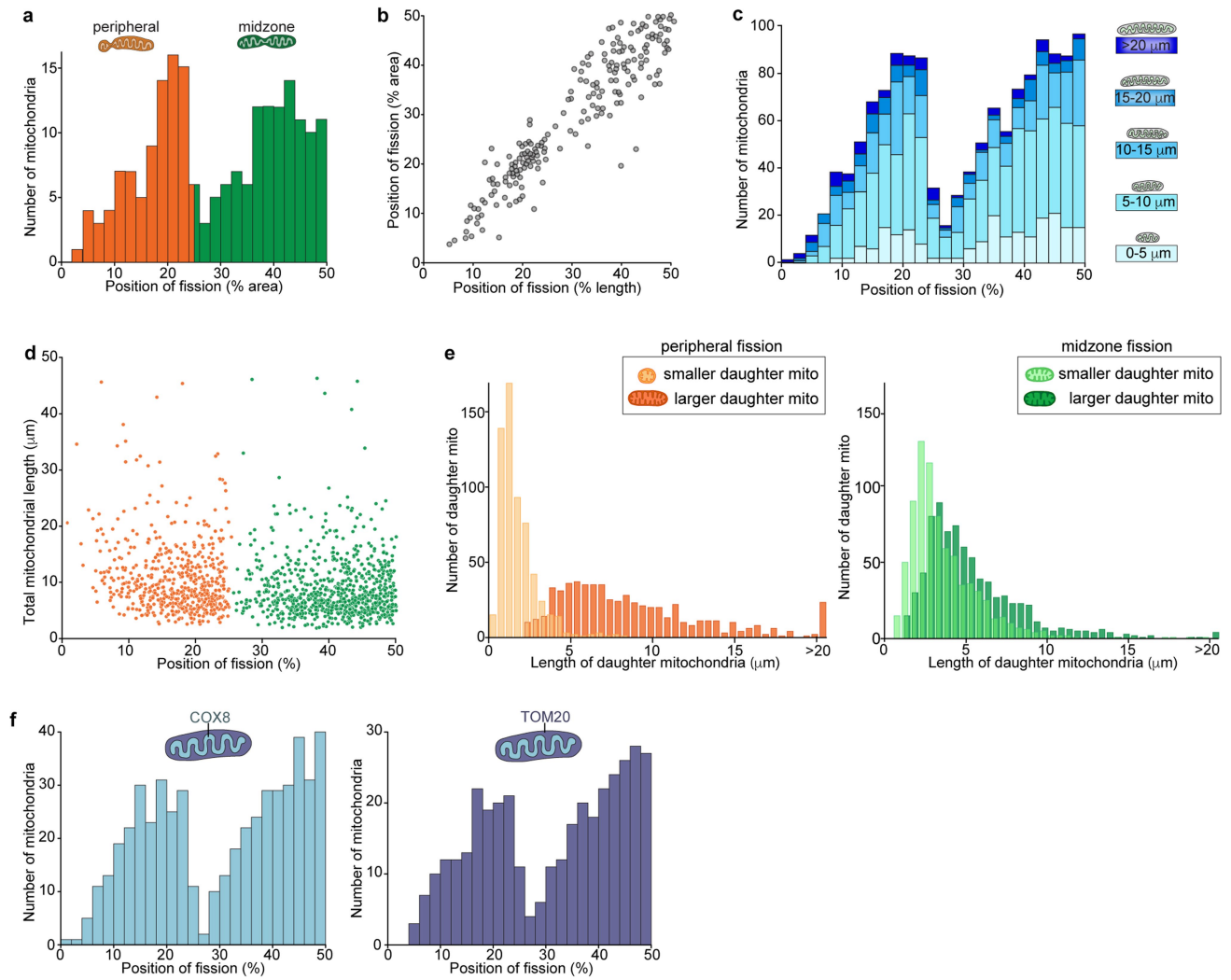
Extended Data Fig. 1 | Distribution of mitochondrial fission sites. a, Histogram of the relative position of constriction/fission measured by mitochondrial volume (*n* = 190 fissions). The two peaks are coloured in orange (0–25 bin; 'peripheral position') and green (25–50 bin; 'midzone position'). **b**, Relative position of mitochondrial fission measured by length versus measured by area (*n* = 190 fissions). **c**, Stacked histogram of the relative position of fission for different bins grouped by the total length of the dividing mitochondria (*n* = 1393). **d**, Scatter plot of the total length of dividing mitochondria versus the relative position of the fission site along the length axis with peripheral fissions (0–25% bin) coloured in orange and midzone fissions (25–50% bin) coloured in green (*n* = 1393 fissions). **e**, Length distribution of the smaller (light colour) and larger (dark colour) daughter mitochondria arising from peripheral left, orange) and midzone (right, green) fissions. **f**, Histogram of relative position of fission in datasets acquired with a mitochondrial inner membrane marker (left, COX8 targeting domain; *n* = 510 fissions) and a mitochondrial outer membrane marker (right, TOM20; *n* = 368 fissions).
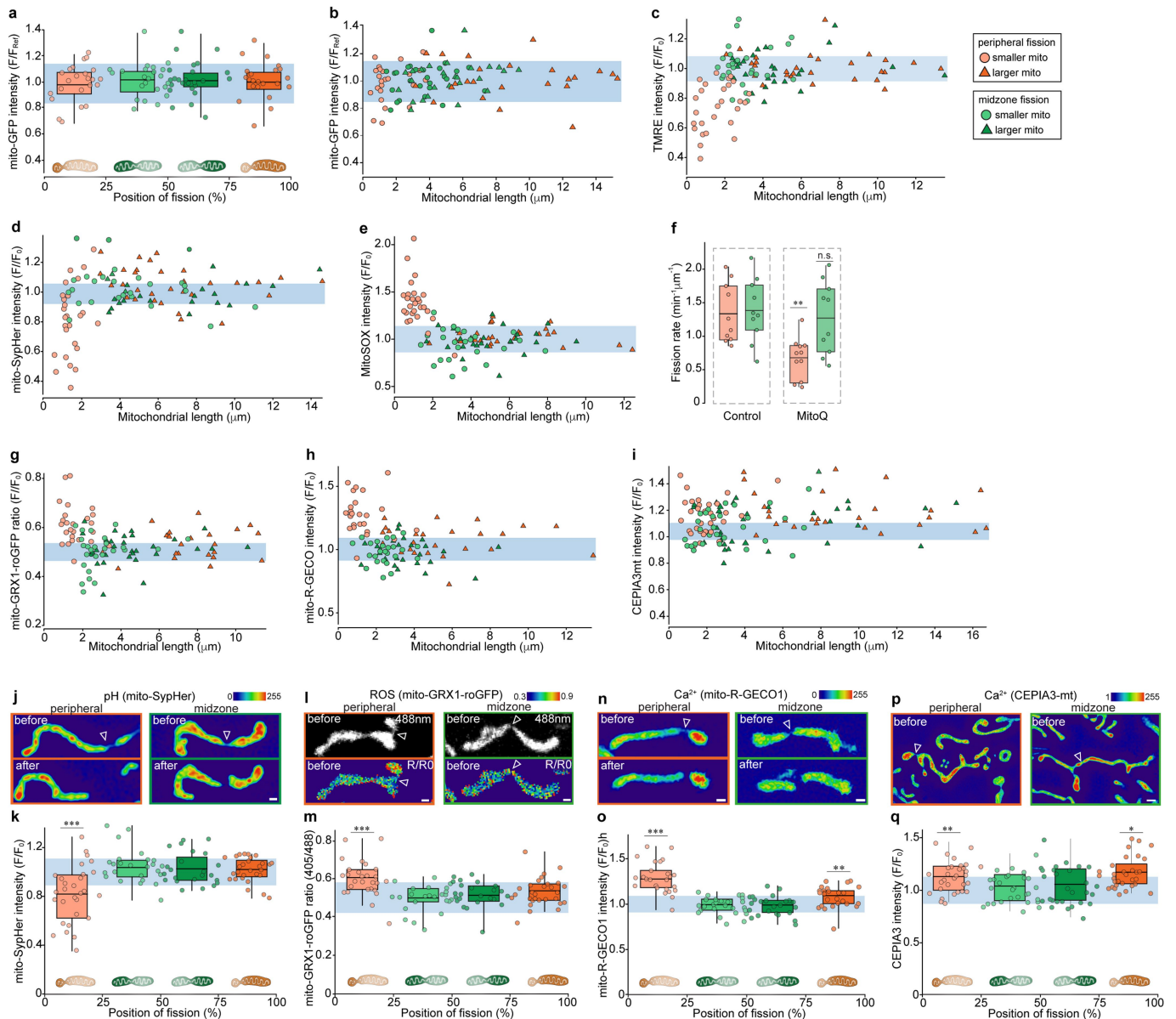
Extended Data Fig. 2 | Physiological changes preceding fission are independent of volume and absolute length. a, Normalized mito–GFP intensity depending on the relative position of fission measured in mitochondria immediately before fission. (n = 50 fissions). **b**, Dependence on the length of the daughter mitochondria of normalized mito–GFP intensity immediately before peripheral (orange) or midzone (green) fissions (n = 50 fissions). **c**, Dependence on the length of the daughter mitochondria of normalized TMRE intensity immediately before peripheral (orange) or midzone (green) fissions (n = 56 fissions). **d**, Dependence on the length of the daughter mitochondria of normalized mito–SypHer intensity before fission (n = 53 fissions). **e**, Dependence of the length of the daughter mitochondria on normalized MitoSOX intensity before fission (n = 52 fissions). **f**, Rates of peripheral and midzone fissions in control Cos-7 cells (n = 10 fields of view) versus cells treated with 500 nM ROS scavenger MitoQ (n = 10 fields of view). **g**, Dependence on the length of the daughter mitochondria of ratiometric intensity of mito–GRX1–roGFP immediately before fission (n = 52 fissions). **h**, Dependence on the length of the daughter mitochondria of normalized mito–R-GECO1 intensity before fission (n = 50 fissions). **i**, Dependence on the length of the daughter mitochondria of normalized CEPIA3–mt intensity before fission (n = 61 fissions). **j**, Mitochondrial pH before and after a peripheral

or midzone fission from SIM movies of mito–SypHer transfected Cos-7 cells. **k**, Normalized mito–SypHer intensity as a function of relative position of fission, measured immediately before fission (n = 53 fissions). **l**, Mitochondrial ROS before and after a peripheral or midzone fission from ratiometric images of mito–GRX1–roGFP transfected Cos-7 cells. **m**, Ratiometric mito–GRX1–roGFP intensity as a function of relative position of fission, measured immediately before fission (n = 52 fissions). **n**, Mitochondrial matrix Ca^{2+} before and after a peripheral or midzone fission from SIM movies of mito–R-GECO1 transfected Cos-7 cells. **o**, Normalized mito–R-GECO1 intensity as a function of relative position of fission, measured immediately before fission (n = 50 fissions). **p**, Mitochondrial matrix Ca^{2+} before and after a peripheral or midzone fission from SIM movies of CEPIA3–mt transfected Cos-7 cells. **q**, Normalized CEPIA3–mt intensity as a function of relative position of fission, measured immediately before fission (n = 61 fissions). In **a**, **k**, **m**, **o** and **q** circles indicate individual measurements; values of binned groups represented as box plots (line, mean; bounds of box: 25th and 75th percentiles; whiskers, min/max values). Light blue areas indicate mean intensity in non-dividing mitochondria (± s.d.). n.s. >0.05, ***P < 0.001. Number of experiments, statistical tests and exact P values are provided in Supplementary Table 1. Scale bars, 0.5 μm. Fission sites are indicated by arrowheads.
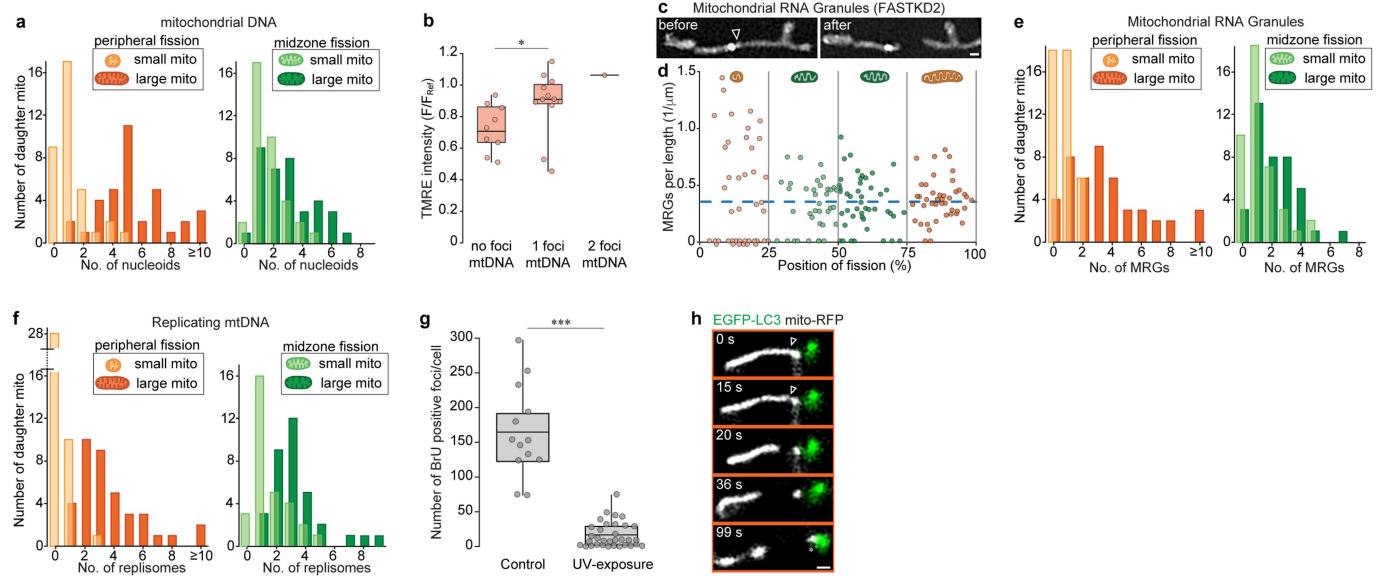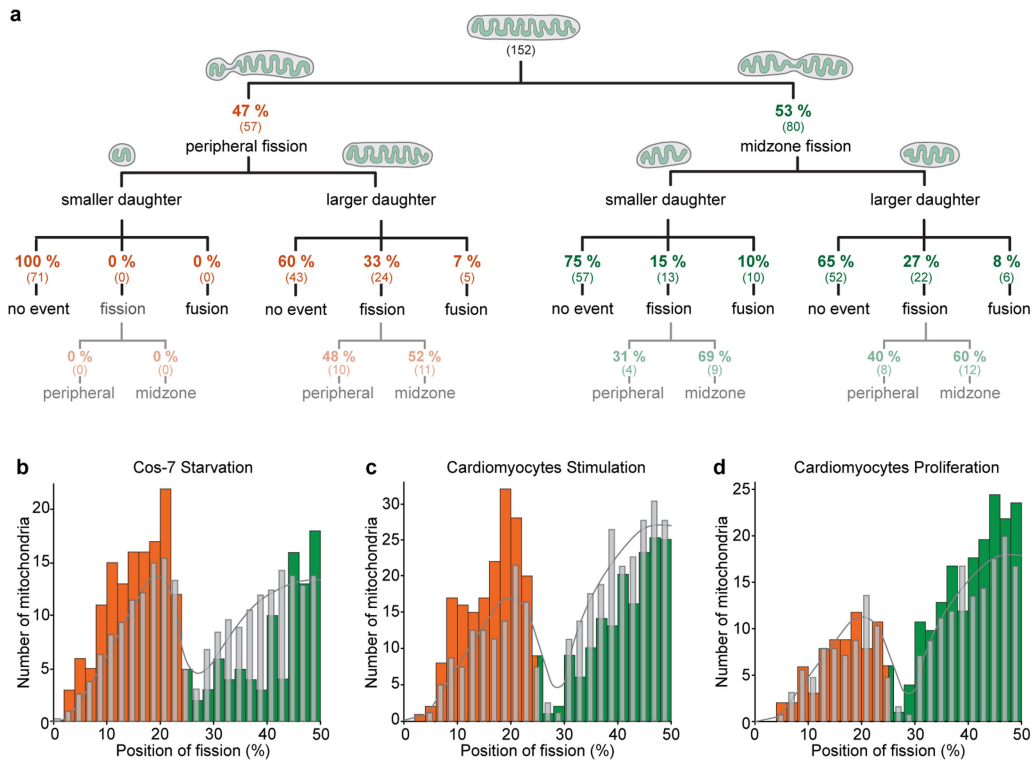
Extended Data Fig. 3 | Redistribution of mitochondrial DNA and RNA granules. a, Distribution of PicoGreen foci in the small and large daughter mitochondrion derived from peripheral and midzone fission ($n = 78$ fissions). **b**, Normalized TMRE intensity in the small daughter mitochondria from peripheral fissions that contain 0, 1 or 2 nucleoids ($n = 20$ fissions). **c**, SIM images of mitochondrial RNA granules (MRGs) (FASTKD2) before and after fission. **d**, Number of MRGs per µm length as a function of fission position ($n = 84$ fissions). Blue line shows average MRG per length in non-dividing mitochondria ($n = 41$). **e**, Distribution of the number of MRGs (FASTKD2; $n = 84$ fissions). **f**, Number of replicating nucleoids (TWINKLE; $n = 74$ fissions) in

smaller (light) and larger (dark) daughter mitochondria from peripheral (orange) and midzone (green). **g**, Number of BrU-positive foci per cell in control Cos-7 cells ($n = 39$) and cells exposed to UV light for 3 min before measurement ($n = 98$). **h**, Time-lapse SIM sequence of Cos-7 mitochondria (mito–RFP, grey) and autophagosomes (EGFP–LC3, green), where the small daughter mitochondrion from a peripheral fission is being taken up by an autophagosome (asterisk). In **b** and **g** circles indicate individual measurements; line, mean; bounds of box, 25th and 75th percentiles; whiskers, min/max values. $*P < 0.05$, $***P < 0.001$. Number of experiments, statistical tests and exact P values are provided in Supplementary Table 1. Scale bars, 0.5 µm.
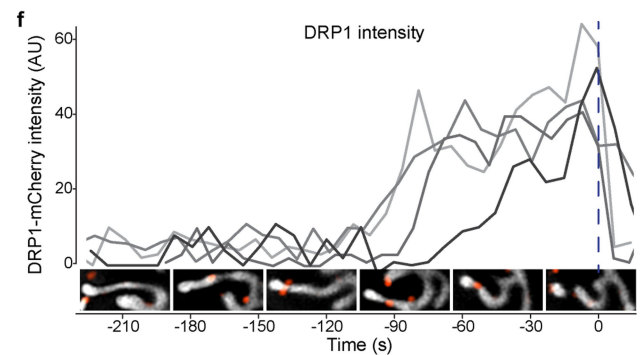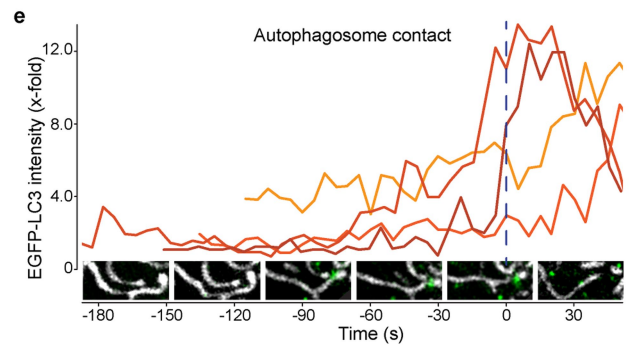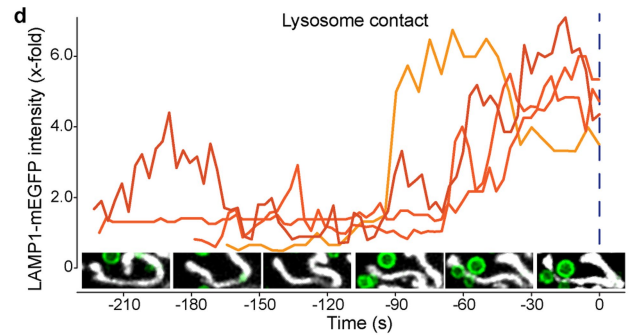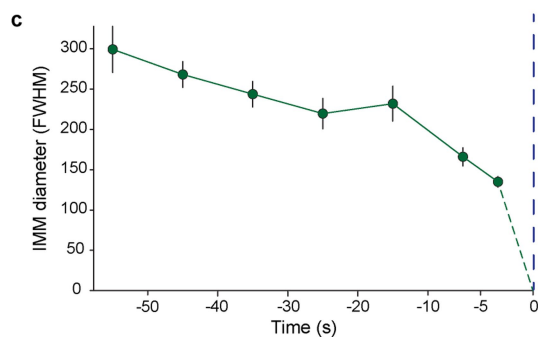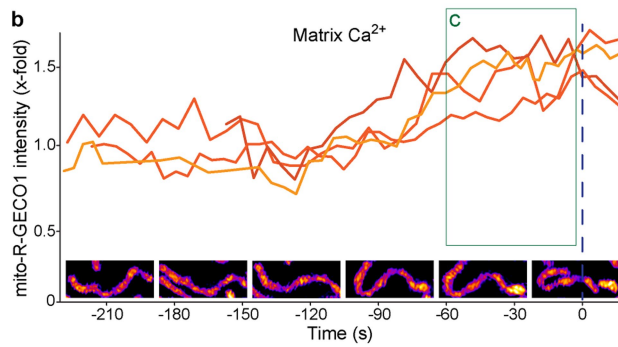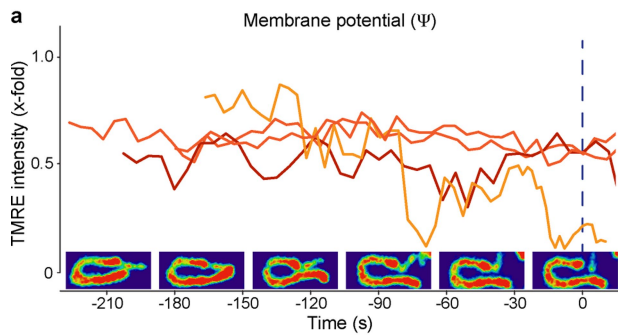
Extended Data Fig. 4 | Time course of physiological changes and recruitment of fission regulators. a, **b**, Time course of fluorescent signals in four examples of Cos-7 mitochondria displaying normalized TMRE intensity (**a**) and mito–R-GECO1 intensity (**b**) with corresponding SIM images in the mitochondrial compartment giving rise to the smaller daughter mitochondria before a peripheral division. **c**, Average inner membrane diameter at the constriction site at several time points before fission, measured in mito–R-GECO1 transfected Cos-7 cells during the time window where Ca^{2+} is elevated (green box in **b**, $n = 10$ fission events). **d**, **e**, Time course of lysosome co-localization (**d**) and autophagosome co-localization (**e**) at constriction sites for peripheral fissions, by measuring LAMP1–mEGFP and EGFP–LC3 intensity, respectively. For EGFP–LC3 measurements, cells were pre-treated with 10 μM CCCP to increase LC3 signals. **f**, Normalized DRP1 intensity at the constriction sites before peripheral fission in four examples of Cos-7 mitochondria with corresponding SIM images. Blue dotted lines ($t = 0$ s) mark the time point of fission.

Extended Data Fig. 5 | Peripheral and midzone fissions interact differently with the mitochondrial network, and the distribution of the fission positions is regulated independently. a, Schematic diagram depicting the fate ('no event', another 'fission' or 'fusion') of each daughter mitochondrion from peripheral and midzone fissions after the initial division in postnatal cardiomyocytes. Only mitochondria that could be traced for more than 100 s after fission were included in the analysis. **b**, Distribution of the relative position of fission in starved Cos-7 cells, with peripheral (1–25%) fission labelled in orange and midzone fissions (25–50%) in green (*n* = 212 fissions). The frequency distribution of Cos-7 control samples is superimposed in grey (replotted from Fig. 1c). **c**, **d**, Distribution of the relative position of constriction/fission along the length axis of isoproterenol-treated mouse cardiomyocyte mitochondria (**c**; *n* = 356 fissions) and miR-199 treated cardiomyocytes (**d**; *n* = 225 fissions) respectively. The frequency distribution of untreated mouse cardiomyocyte samples is superimposed in grey (replotted from Fig. 1e).
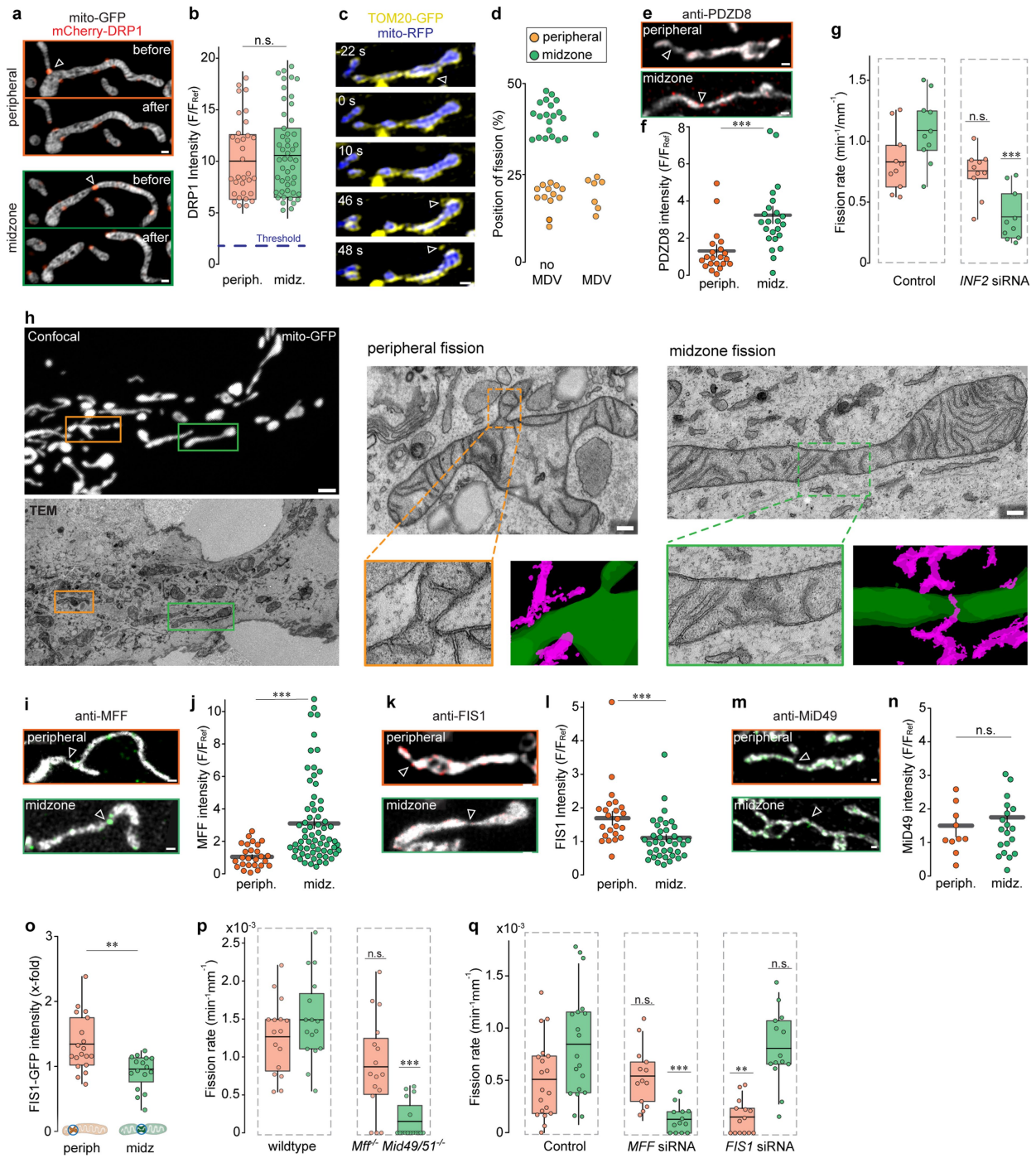
Extended Data Fig. 6 | See next page for caption.

Article

Extended Data Fig. 6 | Peripheral and midzone fissions are both DRP1 mediated but involve distinct upstream mechanisms. a, Two-colour SIM images of mitochondria (mito–GFP, greyscale) and DRP1 (mCherry–DRP1, red) undergoing peripheral or midzone fission. **b**, Normalized DRP1 intensity on the constriction sites of peripheral and midzone divisions. The threshold for a DRP1 accumulation (blue dotted line) was set at a signal >3× over background ($n=107$ fissions). **c**, Time-lapse sequence of a SIM movie, in which both mitochondrial outer membrane (TOM20–GFP) and inner membrane (mito–RFP) were labelled to detect mitochondria-derived vesicle (MDV) formation (arrowhead). **d**, Quantification of the fission positions for mitochondria undergoing MDV formation or not before or after division ($n=41$ fissions). **e**, SIM images of peripheral and midzone constrictions in fixed Cos-7 cells labelled with anti-PDZD8 (red). **f**, Distribution of normalized fluorescence intensities of anti-PDZD8 staining in fixed Cos-7 cells for peripheral (orange) and midzone (green) fissions ($n=38$ fissions). **g**, Rate of peripheral and midzone fissions in control cells ($n=10$ FOV) versus cells treated with *INF2* siRNA ($n=10$ FOV). **h**, Correlated confocal and transmission electron microscopy (CLEM) of mitochondria in Cos-7 cells labelled with mito–GFP, fixed 24 h after expression. Zoom-in of two individual mitochondria with a peripheral (orange frame) and a midzone (green frame) constriction in the TEM plane containing the widest diameter of the constriction site. Pseudo-colouring of three consecutive TEM *z*-sections recombined into a single rendering shows mitochondria (green) and ER (magenta). Scale bar represents 2 μm in confocal and 200 nm in TEM images. **i**, **k**, **m**, SIM images of peripheral and midzone constrictions in fixed Cos-7 cells labelled with anti-TOM20 (grey) and anti-MFF (green) (**i**), anti-FIS1 (red) (**k**) and anti-MiD49 (green) (**m**). **j**, **l**, **n**, Distribution of normalized fluorescent intensities of anti-MFF ($n=92$ fissions) (**j**), anti-FIS1 ($n=59$ fissions) (**l**) and anti-MiD49 ($n=29$ fissions) (**n**) staining in fixed Cos-7 cells for peripheral (orange) and midzone (green) fissions. **o**, Normalized FIS1–GFP intensity at the fission site of peripheral (left) and midzone (right) divisions (orange dots: peripheral, green dots: midzone; $n=35$ fissions). **p**, Quantification of the peripheral (orange) and midzone (green) fission rates in wild-type ($n=16$ FOV) and *Mff^{-/-}Mid49^{-/-}Mid51^{-/-}* triple-knockout ($n=16$ FOV) MEFs stained with Mitotracker Green. **q**, Quantification of the peripheral (orange) and midzone (green) fission rates in control Cos-7 cells and cells treated with siRNAs against *MFF* or *FIS1* ($n \geq 13$ FOV per group). n.s. $P > 0.05$, **$P < 0.01$, ***$P < 0.001$. Number of experiments, statistical tests and exact P values are provided in Supplementary Table 1. Scale bars, 0.5 μm. Fission sites are indicated by arrowheads.
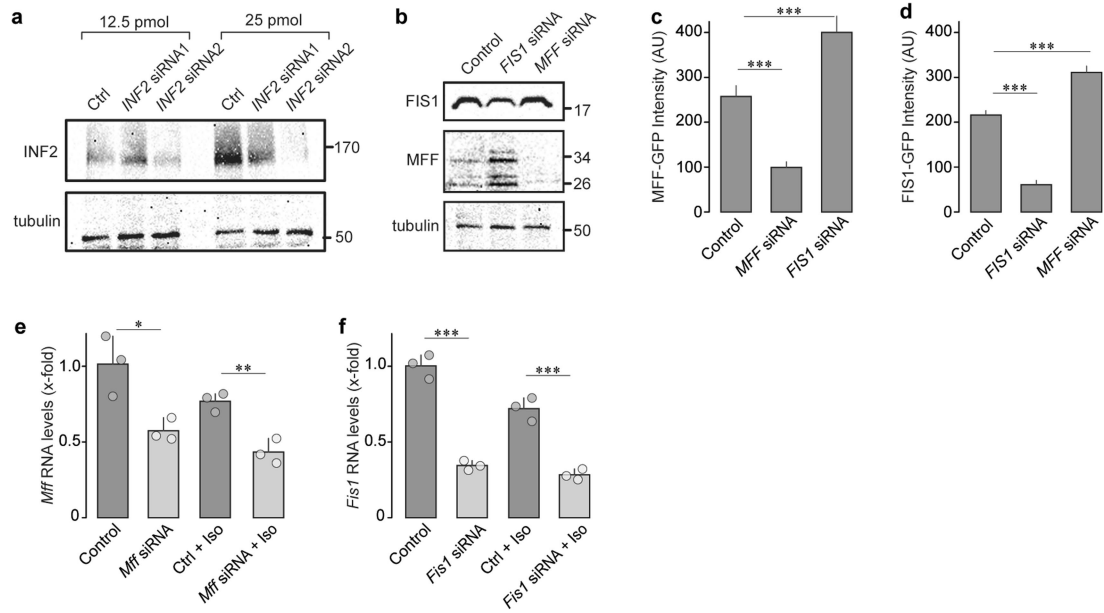
Extended Data Fig. 7 | Silencing efficiency of siRNA against *FIS1*, *MFF* and *INF2* in Cos-7 cells. a, Western blot analysis of protein levels for Cos-7 cells 72 h after transfection with two siRNAs against *INF2* at two different quantities (pmol). Molecular mass is in kilodaltons. **b**, Western blot analysis of protein levels for Cos-7 cells 72 h after transfection with 12.5 pmol of siRNA against *FIS1* or *MFF*. **c**, **d**, Mean fluorescence intensity in U2OS cells endogenously expressing MFF–GFP (**c**) or FIS1–GFP (**d**) in control conditions and 72 h after transfection with siRNA against *FIS1* or *MFF* (*n* > 39 cells per group). **e**, Relative *Mff* RNA expression levels in control cardiomyocytes and in cardiomyocytes 48 h after transfection with si*Mff* and with or without isoproterenol (Iso) treatment. **f**, Relative *Fis1* RNA expression levels in control cardiomyocytes and in cardiomyocytes 48 h after transfection with si*Fis1* and with or without isoproterenol (Iso) treatment. *P < 0.05, **P < 0.01, ***P < 0.00. Number of experiments, statistical tests and exact P values are provided in Supplementary Table 1.

Corresponding author(s):   Suliana Manley, Tatjana Kleele

Last updated by author(s):   Mar 22, 2021

Reporting Summary

Nature Research wishes to improve the reproducibility of the work that we publish. This form provides structure for consistency and transparency in reporting. For further information on Nature Research policies, see Authors & Referees and the Editorial Policy Checklist.

Statistics

For all statistical analyses, confirm that the following items are present in the figure legend, table legend, main text, or Methods section.

n/a	Confirmed	
☐	☒	The exact sample size (*n*) for each experimental group/condition, given as a discrete number and unit of measurement
☐	☒	A statement on whether measurements were taken from distinct samples or whether the same sample was measured repeatedly
☐	☒	The statistical test(s) used AND whether they are one- or two-sided *Only common tests should be described solely by name; describe more complex techniques in the Methods section.*
☒	☐	A description of all covariates tested
☐	☒	A description of any assumptions or corrections, such as tests of normality and adjustment for multiple comparisons
☐	☒	A full description of the statistical parameters including central tendency (e.g. means) or other basic estimates (e.g. regression coefficient) AND variation (e.g. standard deviation) or associated estimates of uncertainty (e.g. confidence intervals)
☐	☒	For null hypothesis testing, the test statistic (e.g. *F*, *t*, *r*) with confidence intervals, effect sizes, degrees of freedom and *P* value noted *Give P values as exact values whenever suitable.*
☒	☐	For Bayesian analysis, information on the choice of priors and Markov chain Monte Carlo settings
☒	☐	For hierarchical and complex designs, identification of the appropriate level for tests and full reporting of outcomes
☒	☐	Estimates of effect sizes (e.g. Cohen's *d*, Pearson's *r*), indicating how they were calculated

Our web collection on statistics for biologists contains articles on many of the points above.

Software and code

Policy information about availability of computer code

Data collection	iSIM data were acquired using Micromanager 2.0 beta and Matlab 2016b. SIM data were acquired using NIS Element (v 3.2.2.) Confocal data were acquired using Zeiss ZEN (V 6.0.0.) and Leica LAS X (v. 3.5.2)
Data analysis	Raw SIM images were reconstructed using Nikon NIS-Elements software (with recommended settings). Raw iSIM images were deconvolved using the Lucy-Richardson deconvolution algorithm (Richardson WH, 1972; Lucy LB, 1974) implemented in MATLAB, and were run for 40 iterations. Reconstructed/ deconvolved images were analyzed using ImageJ/Fiji (1.53c, Java 1.8.0_172 64bit) BrU quantification was performed via a custom written Fiji macro script (available at https://github.com/TimoHenry/MitochondrialRNAgranules) Caspase stainings were analyzed with a custom written Fiji macro script (available at https://github.com/jutziw/mitochondrial_division) All graphs and statistics were performed using OriginPro 2020b

For manuscripts utilizing custom algorithms or software that are central to the research but not yet described in published literature, software must be made available to editors/reviewers. We strongly encourage code deposition in a community repository (e.g. GitHub). See the Nature Research guidelines for submitting code & software for further information.

Data

Policy information about availability of data

All manuscripts must include a data availability statement. This statement should provide the following information, where applicable:
- Accession codes, unique identifiers, or web links for publicly available datasets
- A list of figures that have associated raw data
- A description of any restrictions on data availability

All images displayed as well as numerical data are publicly available on the online repository Zenodo (https://doi.org/10.5281/zenodo.3550643). The unprocessed Western blot gels are provided in Supplementary Figure 1. Custom written Fiji macros are available in the online repository Github (https://github.com/TimoHenry/

MitochondrialRNAgranules and https://github.com/jutziw/mitochondrial_division). Plasmids and cell lines are available to share, do not hesitate to contact the corresponding authors.

Field-specific reporting

Please select the one below that is the best fit for your research. If you are not sure, read the appropriate sections before making your selection.

☒ Life sciences ☐ Behavioural & social sciences ☐ Ecological, evolutionary & environmental sciences

For a reference copy of the document with all sections, see nature.com/documents/nr-reporting-summary-flat.pdf

Life sciences study design

All studies must disclose on these points even when the disclosure is negative.

Sample size	No statistical method was used to predetermine sample size. Sample size was chosen to achieve statstical significance, according to our previous experience and other studies from the field (e.g. Lee et al., Nature 2016, 540, pages139–143)
Data exclusions	Imaging data were excluded if image quality was poor or if the cell and mitochondria displayed signs of stress (round, immobile mitochondria). No data was excluded at the analysis stage.
Replication	Each experiment was reproduced in at least 2 independent experiments and multiple replicates were performed for each experiment. Please refer to figure legends and methods for details. All replications were successful.
Randomization	For studies involving multiple experimental conditions, studies were performed on cells originating from the same cell line batch and were randomly allocated in different wells and randomly assigned to different experimental conditions. No additional randomization was applicable for our experiments.
Blinding	Blinding was not applicable for most datasets, since all cells were cultured under the same conditions and analyzed using the same methods. Experiments containing group allocations were performed blinded (Data from Fig. 3a, b, k) since the treatment of the sample was not revealed to the analyzing individual or an automated analysis was performed (Fig. 3i,j)

Reporting for specific materials, systems and methods

We require information from authors about some types of materials, experimental systems and methods used in many studies. Here, indicate whether each material, system or method listed is relevant to your study. If you are not sure if a list item applies to your research, read the appropriate section before selecting a response.

Materials & experimental systems

n/a	Involved in the study
☐	☒ Antibodies
☐	☒ Eukaryotic cell lines
☒	☐ Palaeontology
☐	☒ Animals and other organisms
☒	☐ Human research participants
☒	☐ Clinical data

Methods

n/a	Involved in the study
☒	☐ ChIP-seq
☒	☐ Flow cytometry
☒	☐ MRI-based neuroimaging

Antibodies

Antibodies used	All used antibodies are listed in the Methods section and were commercially available. Antibodies for Western blots: anti-Fis1 (LuBioScience GmbH, 10956-1-AP, diluted 1:2000), anti-Mff (Life Technologies, PA5-52765, diluted 1:500-1:1000), anti-Inf2 (Sigma-Aldrich HPA000724, diluted 1:2000), anti-alpha-Tubulin (Santa Cruz sc-5286, diluted 1:2000). Antibodies for fluorescent imaging: anti-bromodeoxyuridine (BrdU) (Roche 11170376001; 1:250 to 1:500 dilution), Fis1 polyclonal antibody (Proteintech 109561-AP, Lot# 00048564, 1:50 dilution), Mff (C2orf33) polyclonal antibody (Life Technologies PA567357, Lot# R110001 and TH2624918A, 1:50 dilution), PDZD8 polyclonal antibody (Life Technologies PA553368, Lot# A116318, 1:50 dilution), Mid49 (SMCR7) polyclonal antibody (Life Technologies, PA559950, Lot# G116392, 1:50 dilution), TOM20 mouse monoclonal antibody (Santa Cruz sc-17764, 1:50 dilution). Alexa fluorophore-conjugated secondary antibodies from Life Technologies were diluted 1:1000
Validation	Life Technologies: Invitrogen antibodies are currently undergoing a rigorous 2-part testing approach Part 1—Target specificity verification: This helps ensure the antibody will bind to the correct target. Our antibodies are being tested using at least 1 of the following methods to ensure proper functionality in researcher's experiments. Knockout, Knockdown, Independent antibody verification (IAV), Cell treatment, Relative expression, Neutralization, Peptide array, SNAP-ChIP™, Immunoprecipitation-Mass Spectrometry (IP-MS)

Part 2—Functional application validation: These tests help ensure the antibody works in a particular application(s) of interest, which may include: Western blotting, Flow cytometry, ChIP, Immunofluorescence imaging, Immunohistochemistry
1. anti-Mff/ C2orf33 (Life Technologies PA567357): Applications: WB, ICC, IF (used for IF in our study)
2. anti-Mff (Life Technologies, PA5-52765): Applications: WB, IHC, ICC, IF (used for WB in our study)
3. anti-Mid49/ SMCR7 (Life Technologies, PA559950): Applications: IHC (used for IF in our study)
4. anti-PDZD8 (Life Technologies PA553368): Applications: IHC, ICC, IF (used for IF in our study)

Proteintech: We use affinity chromatography, which makes use of the binding strength of a protein for its ligand. Another popular method is protein A/G purification, which uses the recombinant fusion protein A/G from E.coli. Protein A/G purification will yield all IgGs in the serum, not just the desired antibodies. Affinity chromatography selects for just the ones with the highest affinity toward the target. We also validate our antibodies through knockout and knockdown (KO/KO) studies. Proteintech was the first company to implement siRNA knockdown validation experiments, the gold standard for testing antibody specificity. The validation process involves using small interfering RNA to knock down gene expression in an antibody product - assessing whether the signal subsides with the expression of the target gene.
1. Fis1 polyclonal antibody (109561-AP): Applications: WB, IP, IHC, IF,ELISA (used for IF in our study)

Sigma-Aldrich: All Prestige Antibodies Powered by Atlas Antibodies are developed and validated by the Human Protein Atlas (HPA) project (www.proteinatlas.org).
1. anti-Inf2 (Sigma-Aldrich HPA000724): Enhanced validation by orthogonal RNAseq. Applications: IHC (used for WB in our study)
2. anti-bromodeoxyuridine/ BrdU (Sigma/ Roche 11170376001): The antibody specifically binds to bromodeoxyuridine and crossreacts with iodouridine (10%). Anti-bromo-deoxyuridine does not crossreact with fluorodeoxy-uridine, nor with any endogenous cellular components such as thymidine or uridine. Applications : FC, IHC, IF (used for IF in our study)

Santa Cruz Biotech: Validated by knckdown + WB and by WB, IF etc. in >300 publications
1. anti-TOMM20 (Santa Cruz sc-17764): Applications : IP, ELISA, IF, IHC, WB (used for IF in our study)
2. anti-alpha-Tubulin (Santa Cruz sc-5286) : Applications : WB, IP, IF, IHC(P), FCM and ELISA (used for WB in our study)

LuBioScience GmbH
1. anti-Fis1 (LuBioScience 10956-1-AP): Orthogonal validation by siRNA knockdown Applications: ELISA, IF, IHC, IP, WB (used for WB in our study)

Eukaryotic cell lines

Policy information about cell lines

Cell line source(s)	COS7 - ECACC - 87021302; U2OS-ECACC- 92022711; HEK293T - ATCC - CRL-11268 MEFs were generated by the laboratory of Mike Ryan (see Osellame et al, J Cell Sci, 2016): Mouse embryonic stem cell (ESC) lines containing a gene-trap disruption of smcr7 (MiD49) were obtained from the Knockout Mouse Project (KOMP) Repository (project ID: VG10452). The ESCs were injected into blastocysts to generate mouse lines in C57Bl/6N mice (Australian Phenomics Network). MEFs lacking MiD49 were generated from mid-gestation (E10.5 day) embryos from heterozygotes mating pairs. All experiments were performed in accordance with Animal Ethics Committee approval (Monash and La Trobe Universities). TALEN pairs were generated against the following genes in the indicated genomic regions: Mff target site, exon 1, 5'-GCTGAGATGGCAGAA-3'; and Fis1 target site, exon 2, 5'-AGAATTTTGAAAGGAAATTTC-3'. ΔDrp1 MEFs were generated using the CRISPR/Cas9 system (Ran et al., 2013). The target site was determined through gene analysis using CHOPCHOP (Montague et al., 2014). The Drp1 target site was exon 1, 5'-GCAGGACGTCTTCAACACAG-3. TALEN pairs for MiD51 were as reported previously (Richter et al., 2014). TALEN and CRISPR/Cas9 cell lines were sorted through fluorescence (GFP and mCherry for TALEN pairs, GFP for CRISPR/Cas9) flow cytometry to give single cells to ensure clonality. Genomic verification of all cell lines was performed as reported previously (Stroud et al., 2013). Control MEFs were used as controls. The indels generated are shown in http://jcs.biologists.org/lookup/suppl/doi:10.1242/jcs.185165/-/DC1. Commonly misidentified cells: Not applicable as no commonly misidentified cell lines were used in the study.
Authentication	ECACC uses STR profiling for authentication. ATCC uses STR profiling for authentication.
Mycoplasma contamination	The used cell line is routinely tested for mycoplasma contamination and cells are typically discarded if positive.
Commonly misidentified lines (See ICLAC register)	We did not use commonly misidentified cell lines.

Animals and other organisms

Policy information about studies involving animals; ARRIVE guidelines recommended for reporting animal research

Laboratory animals	Species: Mus musculus; Strain: C57Bl6/J; Age: P1; Sex: male and female. Mice were housed in a 12-hour light / 12-hour dark cycle at a temperature of 23oC with 40 to 60% humidity.

Wild animals	no wild animals were used in this study
Field-collected samples	no field-collected samples were used in this study
Ethics oversight	Animal experiments were approved by the Government Veterinary Office (Lausanne, Switzerland) and performed according to the University of Lausanne Medical School institutional guidelines.

Note that full information on the approval of the study protocol must also be provided in the manuscript.